AGU PUBLICATIONS

Tectonics

RESEARCH ARTICLE
10.1002/2017TC004702

Key Points:
- The lithospheric mantle beneath the Styrian Basin is mostly composed by highly annealed amphibole-bearing spinel peridotites
- Crystal-preferred orientations of olivine are consistent with lithospheric deformation accommodated by dislocation creep in a transpressional regime
- Correlation between microstructures and hydroxyl contents in olivine suggests that annealing was triggered by percolation of fluids/melts

Supporting Information:
- Supporting Information S1
- Figure S1
- Figure S2
- Figure S3
- Figure S4
- Figure S5
- Table S1

Correspondence to:
C. Szabó,
cszabo@elte.hu

Citation:
Aradi, L. E., Hidas, K., Kovács, I. J., Tommasi, A., Klébesz, R., Garrido, C. J., & Szabó, C. (2017). Fluid-enhanced annealing in the subcontinental lithospheric mantle beneath the westernmost margin of the Carpathian-Pannonian extensional basin system. *Tectonics*, *36*, 2987–3011. https://doi.org/10.1002/2017TC004702

Received 20 JUN 2017
Accepted 10 NOV 2017
Accepted article online 21 NOV 2017
Published online 13 DEC 2017

Fluid-Enhanced Annealing in the Subcontinental Lithospheric Mantle Beneath the Westernmost Margin of the Carpathian-Pannonian Extensional Basin System

L. E. Aradi[1], K. Hidas[2], I. J. Kovács[3,4], A. Tommasi[5], R. Klébesz[6], C. J. Garrido[2], and C. Szabó[1]

[1]Lithosphere Fluid Research Laboratory, Eötvös Loránd University, Budapest, Hungary, [2]Instituto Andaluz de Ciencias de la Tierra, CSIC and UGR, Granada, Spain, [3]Geological and Geophysical Institute of Hungary, Budapest, Hungary, [4]Now at Geodetic and Geophysical Institute, MTA Research Centre for Astronomy and Earth Sciences, Sopron, Hungary, [5]Géosciences Montpellier, Université de Montpellier and CNRS, Montpellier, France, [6]Geodetic and Geophysical Institute, MTA Research Centre for Astronomy and Earth Sciences, Sopron, Hungary

Abstract Mantle xenoliths from the Styrian Basin Volcanic Field (Western Pannonian Basin, Austria) are mostly coarse granular amphibole-bearing spinel lherzolites with microstructures attesting for extensive annealing. Olivine and pyroxene CPO (crystal-preferred orientation) preserve nevertheless the record of coeval deformation during a preannealing tectonic event. Olivine shows transitional CPO symmetry from [010]-fiber to orthogonal type. In most samples with [010]-fiber olivine CPO symmetry, the [001] axes of the pyroxenes are also dispersed in the foliation plane. This CPO patterns are consistent with lithospheric deformation accommodated by dislocation creep in a transpressional tectonic regime. The lithospheric mantle deformed most probably during the transpressional phase after the Penninic slab breakoff in the Eastern Alps. The calculated seismic properties of the xenoliths indicate that a significant portion of shear wave splitting delay times in the Styrian Basin (0.5 s out of approximately 1.3 s) may originate in a highly annealed subcontinental lithospheric mantle. Hydroxyl content in olivine is correlated to the degree of annealing, with higher concentrations in the more annealed textures. Based on the correlation between microstructures and hydroxyl content in olivine, we propose that annealing was triggered by percolation of hydrous fluids/melts in the shallow subcontinental lithospheric mantle. A possible source of these fluids/melts is the dehydration of the subducted Penninic slab beneath the Styrian Basin. The studied xenoliths did not record the latest large-scale geodynamic events in the region—the Miocene extension then tectonic inversion of the Pannonian Basin.

1. Introduction

The Carpathian-Pannonian region (CPR) is a Miocene Mediterranean-style back-arc extensional basin (e.g., Horváth et al., 2015) situated in central Europe (Figure 1a). Plio-Pleistocene alkaline basalts carried spinel facies lherzolites, sampling extensively the subcontinental lithospheric mantle (SCLM) in this region (e.g., Szabó et al., 2004), which includes both nearly average present-day continental lithosphere thicknesses at the margins of the CPR (>35 km, Horváth et al., 2006) and highly attenuated regions in the middle of the basin. Many studies analyzed xenoliths from volcanic fields both at the margins and the central part of the CPR (Figure 1a). In the western and northern margins, xenoliths from localities in the Styrian Basin Volcanic Field (e.g., Coltorti et al., 2007; Dobosi et al., 2010; Kurat et al., 1980; Vaselli et al., 1996) and in the Nógrád-Gömör Volcanic Field (e.g., Embey-Isztin, 1978; Konecný et al., 1995; Liptai et al., 2017; Szabó & Taylor, 1994) have been studied. In the eastern margin, xenoliths from the Persani Mountains Volcanic Field (e.g., Chalot-Prat & Boullier, 1997; Falus et al., 2008; Vaselli et al., 1995) were studied. In the middle of the basin, xenoliths from the Bakony-Balaton Highland Volcanic Field (e.g., Bali et al., 2008; Berkesi et al., 2012; Créon et al., 2017; Downes et al., 1992; Embey-Isztin, 1976; Embey-Isztin et al., 2001, 1989; Hidas et al., 2010) and the Little Hungarian Plain Volcanic Field were analyzed (e.g., Downes et al., 1992; Embey-Isztin et al., 2001, 1989; Falus et al., 2007). Most of these studies focused on the mineral and whole rock major and trace element geochemistry, Nd-Sr-Pb isotopes, and silicate melt and fluid inclusions in peridotites and pyroxenites (see Szabó et al., 2004, for a review). Only a few report microstructural and crystal-preferred orientation (CPO) data (Falus et al., 2008, 2011; Hidas et al., 2007; Klébesz et al., 2015; Kovács, Falus, et al., 2012;

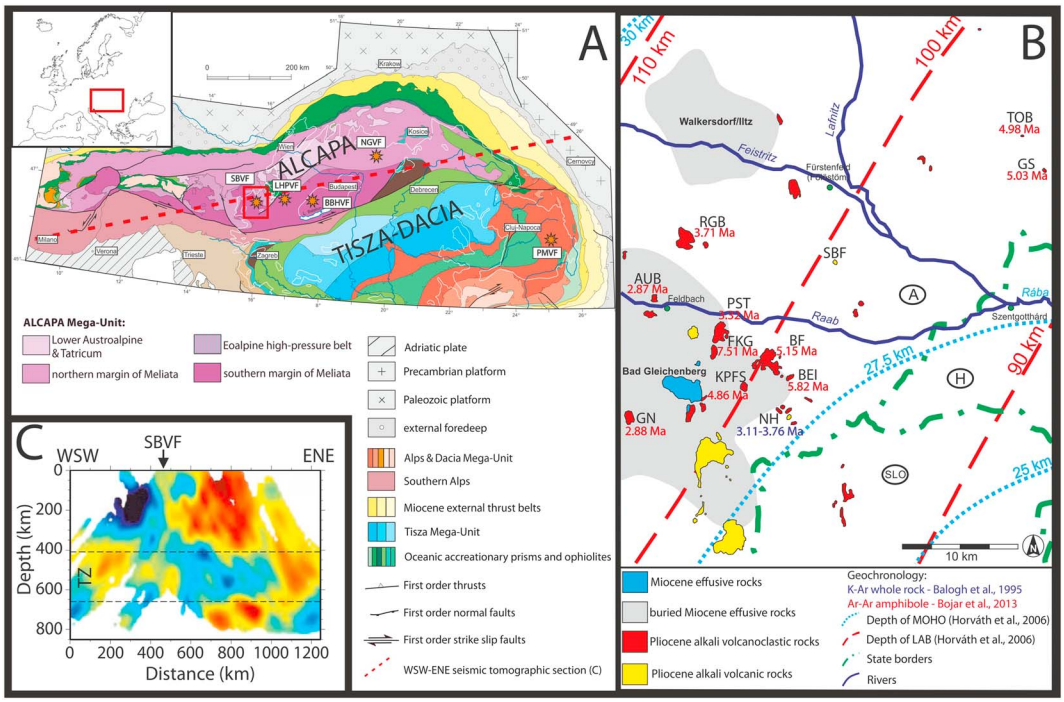

Figure 1. (a) Simplified tectonic map of the Carpathian-Pannonian region and its surroundings (Schmid et al., 2008), showing the location of the volcanic fields containing mantle xenolith-bearing alkaline basalts: Styrian Basin Volcanic Field (SBVF), Little Hungarian Plain Volcanic Field (LHPVF), Bakony-Balaton-Highland Volcanic Field (BBHVF), Nógrád-Gömör Volcanic Field (NGVF), and Persani Mountains Volcanic Field (PMVF). (b) Simplified geological map of the Styrian Basin (Bojar et al., 2013; Kröll, 1988). Geochronological data are from Balogh et al. (1994) and Bojar et al. (2013). The names, their abbrevations, and the coordinates of the sampling localities are included in Table S1 in the supporting information. The depth contours of Moho and LAB are from Horváth et al. (2006). (c) SSW-NNE cross section (red dashed line in Figure 1a) through the tomographic model from Dando et al. (2011). The high-velocity anomaly (blue color) from the lithosphere into the transition zone (TZ) is interpreted as a subducted slab. The approximate position of the SBVF is marked by an arrow.

Liptai et al., 2013). Yet these data are essential for reconstructing the deformation history of the mantle (e.g., Carter & Avé Lallemant, 1970; Karato et al., 2008; Tommasi et al., 1999; Vauchez et al., 2012).

The present study aims to contribute to our knowledge of the thermomechanical evolution of the SCLM beneath the marginal Styrian Basin (SB) by analyzing xenoliths from the Styrian Basin Volcanic Field (SBVF, Figure 1a). Previous studies (Coltorti et al., 2007; Dobosi et al., 2010; Kurat et al., 1980; Vaselli et al., 1996) show that the lithospheric mantle under the SBVF is rather uniform both texturally and geochemically. Coarse-grained, protogranular, and porphyroclastic texture predominate, and the xenoliths exhibit fertile geochemical character. These studies also infer minor amount of metasomatism in the form of CO_2-H_2O-rich subduction-related and mafic alkaline melts (Coltorti et al., 2007; Vaselli et al., 1996).

In this article, we provide CPO data and structurally bonded hydroxyl content of the major constituent phases. We analyzed 33 unaltered mantle xenoliths (3–30 cm large in diameter, Table 1) collected from a lava flow and 12 basaltic tuff, maar, and syneruptively reworked volcanoclastic deposits across the Styrian Basin (Figure 1b; Bojar et al., 2013; Jugovics, 1915, 1916; Pöschl, 1991; Winkler-Hermaden, 1957). Mantle xenoliths from Kapfenstein and Tobaj (e.g., Coltorti et al., 2007; Dobosi et al., 2010; Kurat et al., 1980; Richter, 1971; Vaselli et al., 1996) and lower crustal xenoliths from Beistein (Török et al., 2014) were described before, but this is the first report on mantle-derived xenoliths from the 10 new outcrops (Table S1 in the supporting information). Based on the correlation between microstructures and hydroxyl contents, we propose that fluid-enhanced (including melts) annealing may affect the structurally bonded hydroxyl content in olivine. We attempt to link our data to the results of geophysical surveys and regional geological studies (e.g., Dando et al., 2011; Qorbani et al., 2015) and discuss our conclusions on the light of recent geodynamic models proposed for the region (e.g., Horváth et al., 2015; Kovács, Falus, et al., 2012; Mitterbauer et al., 2011; Qorbani et al., 2015).

AGU Tectonics

10.1002/2017TC004702

Table 1
Petrography, Modal Compositions, Estimated Equilibrium Temperatures, Calculated Parameters, and Calculated Seismic Properties of the Studied SBVF Xenoliths

		Modal composition (%)					Equilibrium temperatures (°C)			Structural hydroxyl content (ppm wt % H_2O)										V_p (km/s)		Avs (%)	
Sample	Lithology	ol	opx	cpx	spl	amph	T_{BK}	T_{CaM}	T_{WES}	ol (Bell)	ol (Kovács)	opx	cpx	bulk	J_{OI}	J_{opx}	J_{cpx}	*BA*	GOS (deg)	minimum	maximum	minimum	maximum
AUB1407	prot lhz	68	18	11	2.5	0.24	1,049	975	979	7.9	4.5	142	408	112	5.0	9.6	9.8	0.40	2.17	7.95	8.6	0.27	5.43
AUB1410	prot lhz	58	26	13	2.3	0.08	1,038	972	1,014	10.8	9.2	183	553	137	7.6	9.5	10.7	0.46	2.24	7.9	8.58	0.04	5.91
BEI1401	amph-rich wbs	34	39	21	1.6	2.46	1,022	999	958	4.8	5.9	201	491	554	4.4	5.6	5.5	0.30	2.26	7.92	8.35	0.17	3.61
BEI1402	prot lhz	45	36	16	3.5	ND	1,056	993	979	8.4	3.7	120	335	100	4.7	9.3	10.0	0.75	1.68	8.02	8.43	0.19	3.99
*BEI1403**	amph-rich wht	63	ND	5	ND	32.4	ND	ND	ND	6.5	6.8	ND	370	4881	6.1	137.7	10.9	0.21	1.42	7.83	8.76	0.42	7.56
BEI1404	prot lhz	69	18	12	1.2	ND	951	908	996	5.2	3.3	105	331	63	6.5	21.7	11.7	0.42	3.67	7.88	8.71	0.27	6.44
BF1411	amph-rich hzb	68	11	5	0.0	15.94	968	937	793	5.9	6.1	ND	ND	2395	4.8	14.6	11.4	0.30	3.90	7.92	8.6	0.12	5.93
FKG1402	prot lhz	60	24	14	0.3	0.45	988	978	966	6.0	5.0	143	423	167	5.3	9.0	8.8	0.41	1.69	7.92	8.48	0.08	4.81
GN1401*	porph lhz	68	19	10	0.9	2.04	896	912	949	7.6	4.1	185	517	397	4.6	6.1	9.4	0.19	2.93	7.93	8.57	0.17	5.85
GN1402	porph lhz	86	8	4	1.7	0.62	944	915	954	8.7	4.4	156	470	130	2.8	10.4	10.7	0.25	2.42	8.08	8.57	0.14	4.41
GN1406*	prot lhz	60	23	14	2.3	0.44	956	939	944	4.8	5.0	196	ND	190	4.3	7.1	8.4	0.32	2.95	7.89	8.52	0.12	5.27
GN1407	amph-rich hzb	66	19	2	0.1	13.21	1,029	942	763	5.7	3.6	ND	544	1985	5.9	8.3	6.3	0.34	3.73	7.85	8.71	0.14	6.75
GN1411	porph lhz	75	18	6	0.9	0.92	906	939	927	6.8	7.6	236	621	220	5.0	6.3	9.3	0.30	2.48	7.88	8.65	0.21	6.55
GN1412*	porph lhz	71	15	12	1.4	0.01	973	944	965	7.1	4.8	159	448	85	5.7	12.6	11.9	0.38	4.18	7.93	8.66	0.37	6.61
GS0610	porph lhz	66	12	21	0.2	ND	1,082	1,113	984	10.3	5.9	102	190	62	3.6	33.7	7.4	0.43	2.22	8.03	8.51	0.17	4.14
GS0611*	fg eq lhz	71	18	9	1.1	0.01	770	801	822	6.3	4.6	124	386	63	1.9	1.5	2.9	0.27	1.10	8.08	8.35	0.02	2.38
GS1408*	porph lhz	58	34	6	2.1	0.01	911	894	967	6.3	5.3	87	297	53	7.4	5.4	10.2	0.13	3.12	7.87	8.45	0.00	6.6
KPFS0402	prot lhz	46	35	17	1.2	0.19	1,053	1,007	1,018	11.3	9.0	290	674	251	5.3	14.5	10.7	0.76	2.27	7.99	8.39	0.12	3.66
KPFS0404*	prot lhz	73	14	12	1.2	0.17	1,027	976	985	10.4	6.7	135	419	126	9.7	19.0	15.7	0.36	3.97	7.88	8.78	0.21	7.15
KPFS0420	prot lhz	70	13	15	1.4	0.04	1,054	986	1,014	7.9	4.8	149	468	105	5.3	7.7	9.0	0.40	2.13	7.91	8.64	0.00	5.9
KPFS0421	prot lhz	55	33	10	2.1	ND	1,047	983	1,006	5.2	3.5	115	366	78	7.4	6.9	13.7	0.58	2.75	7.93	8.62	0.08	6.58
NH0601A*	porph lhz	66	23	10	1.1	ND	860	919	1,007	3.0	7.8	90	240	46	6.1	12.0	8.7	0.26	2.79	7.87	8.61	0.25	6.7
NH1402*	porph lhz	53	27	16	3.2	0.08	967	909	983	5.8	4.4	125	369	109	4.0	7.2	6.9	0.31	3.02	7.97	8.38	0.19	4.38
NH1403	porph hzb	86	11	3	0.1	ND	1,023	984	922	5.4	3.8	84	443	27	6.5	5.9	8.6	0.70	3.31	7.92	8.93	0.37	7.68
NH1408	porph lhz	70	20	10	0.7	0.05	950	895	960	7.5	4.7	154	431	85	5.4	6.5	6.4	0.28	2.81	7.88	8.64	0.02	6.69
PST1401*	prot lhz	58	29	12	0.9	0.01	985	976	1,047	8.7	5.9	208	541	132	4.4	9.3	7.5	0.23	2.35	7.98	8.47	0.23	5.02
PST1403*	porph lhz	63	21	13	3.1	0.02	964	953	1,003	9.4	5.9	185	515	115	5.4	11.1	7.6	0.27	2.77	7.91	8.52	0.21	5.32
RGB1415	porph lhz	78	8	13	0.1	1.76	1,093	966	897	9.2	5.2	157	472	343	7.2	9.9	4.6	0.30	2.91	7.93	8.77	0.41	7.41
RGB1416*	prot lhz	54	15	30	0.9	0.40	941	954	958	8.3	6.5	169	389	206	4.6	8.6	19.6	0.36	2.23	7.92	8.53	0.10	6.46
SBF1401*	porph lhz	74	16	8	2.0	0.07	888	914	1,007	5.3	3.5	85	247	49	5.0	18.8	8.6	0.57	3.77	7.95	8.67	0.14	5.88
TOB1401	porph lhz	56	27	15	2.1	0.53	1,028	966	943	12.8	8.1	269	569	243	3.9	8.9	7.1	0.57	2.29	8.02	8.53	0.23	4.11
TOB1402*	porph hzb	79	17	3	0.5	ND	1,089	1,056	1,053	10.6	7.7	132	326	46	4.7	13.0	13.9	0.73	1.64	7.97	8.79	0.31	7.31
TOB1403*	prot lhz	72	8	9	1.1	8.65	1,013	1,031	949	7.0	4.9	199	580	1374	5.1	8.8	10.1	0.32	1.93	7.91	8.68	0.23	7.81

Note. Samples marked with "*" show clear lineation/foliation. ND: not detected. Samples with names in italic contain rare phlogopite. Abbreviations: lhz: lherzolite, wht: wehrlite, hzb: harzburgite, wbs: websteriteprot: coarse-grained protogranular, porph: coarse-grained porphyroclastic, and fg eq: fine-grained equigranular.

2. Geological Background

The CPR is surrounded by the Bohemian Massif, the East European, and Moesia Platform, the Dinarides, and the Alps (e.g., Csontos & Vörös, 2004; Fodor et al., 1999). It is composed of two tectonic blocks: the ALCAPA (ALps-CArpathian PAnnonian) and the Tisza-Dacia (Figure 1a), which are separated by the Mid-Hungarian Fault Zone (e.g., Bada & Horváth, 2001). The ALCAPA tectonic unit, which contains most xenoliths-bearing volcanic fields (Figure 1a), was extruded from the Alpine-Dinaric region during the Paleogene-Neogene, traveling ~450 km eastward (Kázmér & Kovács, 1985). Some studies elaborated the entire lithosphere (Kovács, Falus, et al., 2012; Kovács & Szabó, 2008), whereas others argue that it only involved the upper crust (e.g., Horváth et al., 2015; Tari & Horváth, 2010). The extrusion of the ALCAPA block, which initiated in the late Oligocene, may have been driven by the extensional collapse of the Eastern Alps and the convergence between the Adriatic indenter and the European Plate (Ratschbacher, Frisch, et al., 1991; Ratschbacher, Merie, et al., 1991). The extrusion was followed by a SSW dipping subduction of oceanic lithosphere of the Carpathian embayment and its rollback in the Eastern Carpathians (e.g., Fodor et al., 1999; Horváth et al., 2015).

In the middle Miocene, extension and lithosphere thinning resulted in melting of a metasomatized lithospheric mantle beneath the Pannonian Basin, producing extensive silicic and calc-alkaline volcanism (Harangi & Lenkey, 2007; Kovács & Szabó, 2008). After subduction ceased in the Eastern Carpathians, the Pannonian Basin became completely landlocked; continued convergence leads to tectonic inversion from the late Miocene to recent times (Fodor et al., 1999; Horváth et al., 2006). This compressional phase resulted in large-scale folding of the lithosphere underneath the Pannonian Basin (Dombrádi et al., 2010). From the late Miocene postextensional alkali basalts erupted to the surface. These basalts were generated by decompressional melting (Embey-Isztin et al., 1993), in response to asthenosphere upwelling from below the adjoining thick lithospheric domains toward the thin spots of the lithosphere (Harangi et al., 2015).

The evolution of the Styrian Basin is closely related to the CPR geodynamics. This basin was developed above an Alpine lithospheric wedge (ALCAPA, Figure 1a), which was extruded eastward during late Oligocene and Miocene times (Ebner & Sachsenhofer, 1995; Ratschbacher, Frisch, et al., 1991; Ratschbacher, Merie, et al., 1991) mentioned above. Rapid and significant uplift of the surface after the onset of tectonic inversion in the late Miocene was also observed in the Styrian Basin (Ebner & Sachsenhofer, 1995).

According to seismic tomographic models (Dando et al., 2011; Lippitsch, 2003; Mitterbauer et al., 2011), evidence for a SWW-NEE oriented fast downwelling structure is observed in the upper mantle beneath the SBVF. This fast anomaly was interpreted as a remnant of the detached Penninic slab (Brückl, 2011; Mitterbauer et al., 2011; Qorbani et al., 2015) or as a detachment of cold, high-velocity lithospheric material sinking into the convective mantle (Dando et al., 2011). In early to middle Miocene, andesitic to shoshonitic magmas erupted in the southeastern part of the basin due to the ongoing extension and lithosphere thinning, which initiated melting in the previously metasomatized lithospheric mantle (e.g., Dobosi et al., 1991; Ebner & Sachsenhofer, 1995; Harangi et al., 1995). The source of this metasomatism was assumed to be the subducted Penninic slab and its dehydration (Harangi et al., 1995). During Pliocene to Pleistocene times, the Styrian Basin was the site of alkali basalt volcanic activity that brought ultramafic xenoliths to the surface (e.g., Ali et al., 2013; Embey-Isztin & Dobosi, 1995; Embey-Isztin et al., 1993; Heritsch, 1967).

3. Analytical Techniques

3.1. Sample Preparation

We prepared double-polished thin sections (thickness between 160 and 620 μm) from the selected unaltered xenoliths. Half of the xenoliths display no visible foliation and/or lineation, and thin slabs were cut at random orientations. For the other half of the samples, where a clear foliation and stretching lineation are defined by the shape-preferred orientation of olivine, spinel, and pyroxene, we prepared thin sections perpendicular to the plane of the foliation and parallel to the lineation (*XZ* plane), fitting the sample on the thin section for exposing the largest area possible. To improve the quality of electron backscatter diffraction (EBSD) measurements, standard diamond paste-polished (down to 1 μm) thin sections were further polished for up to 20 min using colloidal silica suspension. After EBSD analyses, the rock chips were removed from the glass to carry out the Fourier transform infrared (FTIR) analysis.

3.2. Fourier Transform Infrared (FTIR) Spectroscopy

Fourier transformation infrared (FTIR) Spectroscopy (Bruker Varian 600 UMA microscope attached to a Varian 7000 FTIR spectrometer) was used to measure the structurally bond hydroxyl content of the nominally anhydrous minerals (NAMs) in the studied peridotite xenoliths (in rock forming silicates: olivine, clinopyroxene, and orthopyroxene). The measurements were carried out with unpolarized light (Kovács et al., 2008) at the Research Centre for Natural Sciences of the Hungarian Academy of Science in Budapest. To calculate the structural hydroxyl content of the studied minerals, we used the mineral specific calibrations of Bell et al. (1995, 2003). Site-specific calibration was also used to constrain the structurally bond hydroxyl content of olivine (Kovács et al., 2010). The details of the measurements are described in detail in Pintér et al. (2015) and in Text S1 in the supporting information (Balan et al., 2011; Li et al., 2015; Sambridge et al., 2008; Xia et al., 2013).

3.3. Electron Backscattered Diffraction (EBSD)

Crystal-preferred orientation (CPO) of olivine, orthopyroxene, clinopyroxene, and amphibole were obtained by EBSD technique. Diffraction patterns were generated with a JEOL-5600 scanning electron microscope equipped with an Oxford-HKL Technology EBSD system and CHANNEL+ software at Géosciences Montpellier. Kikuchi patterns were obtained using W filament at 17 kV acceleration voltage with a working distance of 23 mm. Complementary EBSD analyses were carried out on a Zeiss EVO MA 15 SEM-EBSD facility of the IACT (Armilla, Spain) using LaB_6 filament with 20 kV acceleration voltage and 24 mm working distance. In both cases the data collection was done using the AZtec 2.4 data acquisition software (Oxford/HKL) with 4×4 binning and low gain settings. EBSD maps that cover an approximately 1.5×2.5 cm rectangle (70–100% of the thin sections) were acquired in automatic acquisition mode with a grid step size of 15–50 μm, depending on the average grain size of the xenolith. In most of the samples indexing rates were above 80%. We applied a segmentation angle of 15° for grain recognition, and the result was controlled visually using EBSD band contrast maps and photomicrographs of the thin sections.

Pole figures were plotted using the careware programs of D. Mainprice (http://www.gm.univ-montp2.fr/PERSO/mainprice/W_data/CareWare_Unicef_Programs/) by using the mean orientation (one point per grain) of each grain to avoid overrepresentation of coarse grains. For straightforward comparison between different samples, the CPO data of the samples where the foliation and lineation were not observed macroscopically were rotated with olivine $[100]_{max}$ east-west and olivine $[010]_{max}$ north-south of the pole figures.

The fabric strength is quantified using the *J*-index of olivine, which is the volume-averaged integral of the squared orientation densities (Bunge, 1982). The *J*-index is dimensionless; it is 1 for a random orientation distribution and infinity for a single crystal orientation. The *J*-index should represent fabric strength correctly if at least 100–150 olivine grains are indexed in per thin sections (Ben Ismail & Mainprice, 1998). Mantle peridotites display *J*-indexes between 2 and 20 with a peak around 5 (Tommasi & Vauchez, 2015). The *J*-index of olivine CPO was calculated using the MTEX toolbox in MATLAB (http://mtex-toolbox.github.io/; Bachmann et al., 2010, Hielscher & Schaeben, 2008; Mainprice et al., 2011) with orientation distribution functions calculated using a "de la Vallée Poussin" kernel with a half width of 10°. To determine the symmetry of the olivine CPO, we used the *BA*-index (Mainprice et al., 2014). The details of the calculation of symmetry indices are described in Text S1 in the supporting information (Mainprice et al., 2014; Michibayashi et al., 2016; Vollmer, 1990).

We estimate the remaining plastic strain in olivine, due to accumulation of dislocations during deformation, by calculating the average misorientation within the grains. From the available parameters in the MTEX toolbox, we chose the average at the thin section scale mis-to-mean (M2M), which is the average deviation of the orientation of a measurement point from the average orientation of the grain (cf. Wright et al., 2011, for a review) of olivine to characterize intragranular deformation. A decrease in M2M values indicates a reduction of intracrystalline misorientations within olivine grains. It allows, therefore, estimating the degree of recrystallization, which can be static (annealing) or dynamic in the xenoliths (e.g., Hidas, Konc, et al., 2016; Tommasi & Ishikawa, 2014).

4. Results

4.1. Textures and Microstructures

The studied xenoliths are predominantly amphibole-bearing lherzolites and amphibole-bearing harzburgites, but an amphibole-rich olivine websterite (xenolith BEI1401) and an amphibole-rich wehrlite

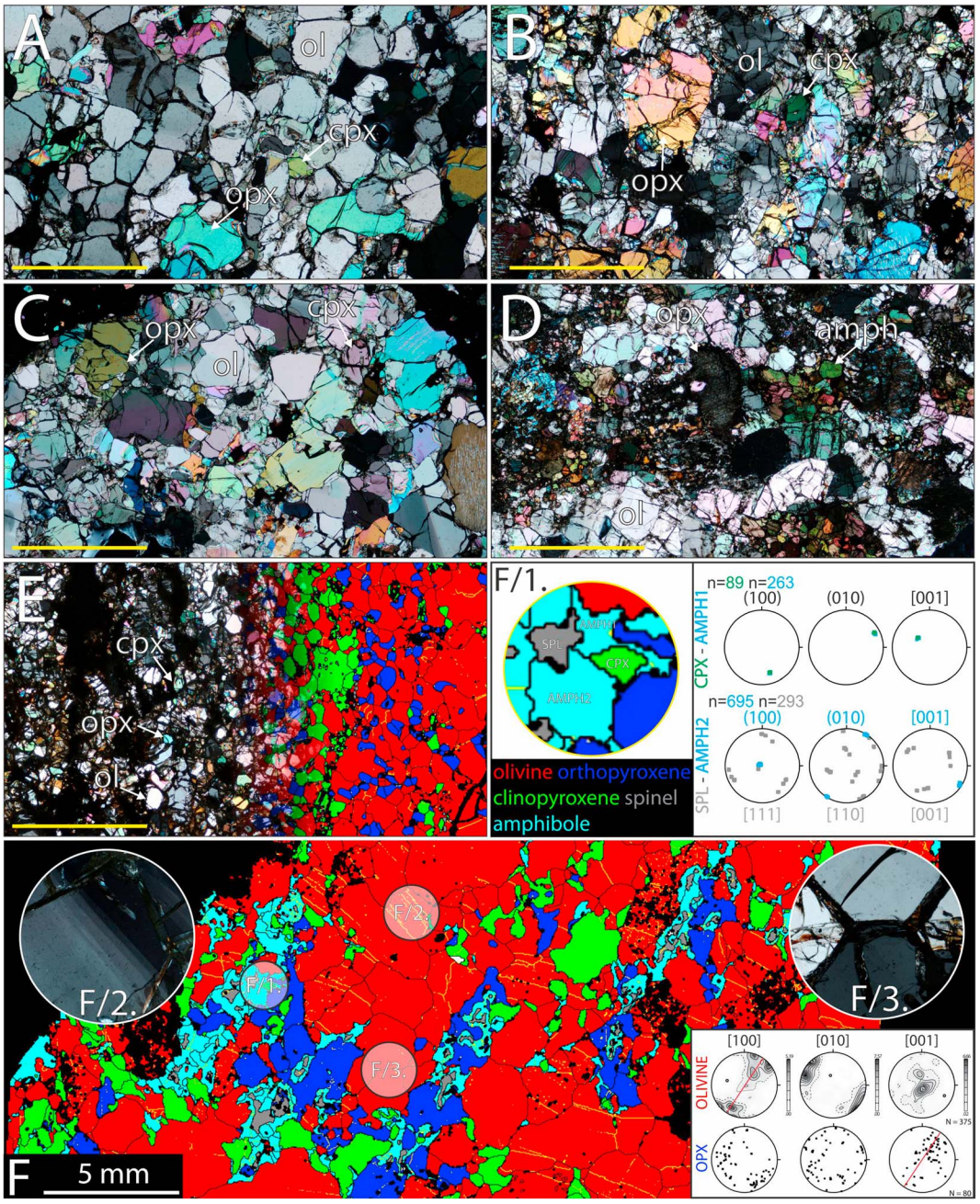

Figure 2. Photomicrographs of representative xenoliths showing coarse-grained protogranular ((a) KPFS0420 lherzolite), coarse-grained porphyroclastic ((b) NH1402 lherzolite and (c) NH0601A lherzolite), amphibole-rich ((d) GN1407 amphibole-rich harzburgite), and fine-grained equigranular ((e) GS0611 lherzolite, overlaid by the EBSD phase map) textures. (f) EBSD phase map of porphyroclastic lherzolite TOB1403. Bottom right inset displays the CPOs of olivine and orthopyroxene in this xenolith. Enlargements illustrate typical microstructural features of this sample: F/1: Pole figures indicating topotaxial overgrowth of amphibole onto clinopyroxene and the relationship between spinel and amphibole orientation in an amphibole-bearing spinel-pyroxene cluster. F/2: Subgrain walls in olivine, perpendicular to the foliation plane. F/3: 120° triple junctions between olivine grains indicate annealing.

(xenolith BEI1403) were also analyzed (Table 1). We classified the texture as protogranular (39% of the sample set), if spinels are in close contact with orthopyroxene and clinopyroxene (Figure 2a) or they form spinel-pyroxene clusters after subsolidus garnet breakdown (cf. Falus et al., 2000) (Figure 2g). We consider the texture as porphyroclastic when the grain size distribution of pyroxenes is bimodal and spinels are

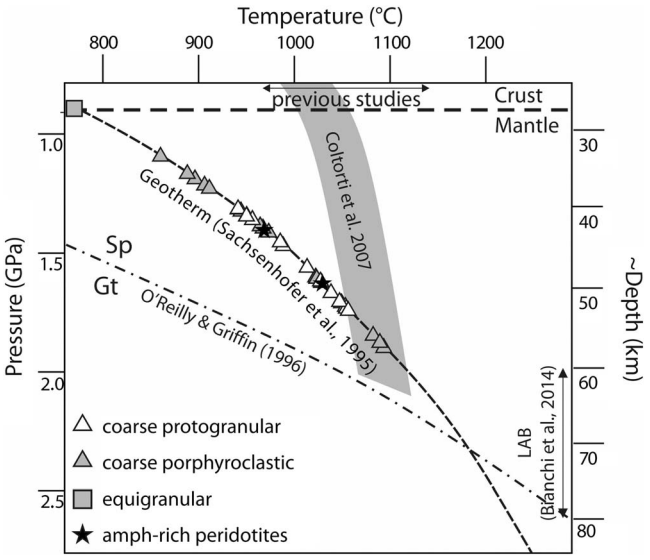

Figure 3. Equilibrium temperatures (T_{BK}) projected onto the recent local geotherm of the Styrian Basin (Sachsenhofer et al., 1997). Spinel (Sp)-Garnet (Gt) phase transformation (dash-dotted line) is from O'Reilly and Griffin (1996). The lithosphere asthenosphere boundary (LAB) depth estimation (60–80 km) is from Bianchi et al. (2014). Crust-mantle boundary (Moho) depth is based on Horváth et al. (2006). The equilibrium temperature range of previous studies is based on the following studies: Kurat et al. (1991, 1980), Vaselli et al. (1996), Dobosi et al. (1999), Falus et al. (2000), and Coltorti et al. (2007). The gray field of Coltorti et al. (2007) shows an estimated paleogeotherm based on equilibrium temperatures and Ca in olivine barometry.

interstitial and/or show holly leaf shapes, or if the pyroxenes show a strong shape-preferred orientation (Figure 2b) (45% of the sample set). Three amphibole-rich samples (BEI1403, BF1411, and GN1407; 12% of the sample set) contain pyroxenes and spinels as minor phases, which hinder the proper textural classification by the above criteria; hence hereafter, we refer to them simply as amphibole-rich peridotites. Finally, the texture of xenolith GS0611 is classified as fine-grained equigranular based on the fine grain size (less than a millimeter) coupled to a penetrative foliation, which is marked by layers enriched in clinopyroxene and by trails of isometric spinels (Figure 2e). Equigranular textures were not reported from the Styrian Basin before.

Irrespective of the textural classification, a uniform petrographic feature of the studied xenoliths is that olivine shows low degrees of intragranular deformation, which is characterized by the almost complete lack of undulose extinction and no evidence for recent dynamic recrystallization. Grain sizes range from $<$850 μm in the fine-grained equigranular xenolith GS0611 to 1,200 μm in the coarse-grained porphyroclastic xenoliths and 2,700 μm in the protogranular ones; the largest olivines are observed in protogranular lherzolite GN1412.

Olivine in all xenoliths has straight to slightly curved boundaries, which often meet in 120° triple junctions. Widely spaced (0.1–1 mm) subgrain walls are locally observed, but they are rare. They tend to be at a high angle to the lineation, when the latter can be observed. Olivine in the fine-grained equigranular xenolith GS0611 shows similar microstructures to those of olivines in coarse-grained xenoliths. Some larger grains in pyroxene-free areas contain rare subgrain boundaries (Figure 2e).

The pyroxenes have curvilinear boundaries. Orthopyroxene typically shows undulose extinction and some kinks. Lamellae of clinopyroxene in orthopyroxene (and vice versa) can be observed in about half of the samples. The clinopyroxenes show little evidence of intracrystalline deformation: subgrain boundaries and undulose extinction are almost absent. In the porphyroclastic xenoliths, the shape-preferred orientation of interstitial and dispersed spinel grains mark a stretching lineation. In some protogranular xenoliths, spinel-pyroxene clusters are elongated, marking a lineation (Figure 2f).

Amphiboles are present in most of the studied xenoliths (25 out of 33), generally in minor amounts ($<$1%) and spatially associated to clinopyroxene and spinel except for the amphibole-rich xenoliths, where they occur interstitially with modal proportions up to 32% (Table 1). Amphiboles are free of intragranular deformation in all studied xenoliths. In the phlogopite-bearing harzburgites BF1411 and GN1407 amphibole replaces pyroxenes and larger clusters of amphibole contain phlogopite and vermicular spinels as inclusions.

4.2. Equilibrium Temperatures

Equilibrium temperatures of the selected xenoliths were calculated with the following geothermometers: two-pyroxene thermometer by Brey and Köhler (1990), Ca in orthopyroxene thermometer by Brey and Köhler (1990), modified by Nimis and Grütter (2010, T_{CaM}), and Cr-Al in orthopyroxene thermometer by Witt-Eickschen and Seck (1991, T_{WES}) (Table 1 and Figure S1 in the supporting information). In Figure 3 we present the results of the two-pyroxene thermometer of Brey and Köhler (1990), which is widely used in the mantle literature, to provide a comparison with published data sets. The T_{BK} equilibrium temperatures are between 860 and 1093°C (±16°C). The only outlier is the fine-grained equigranular xenolith GS0611, which shows the lowest temperatures with all thermometers (T_{BK} = 770°C). Orthopyroxene-based thermometers provide higher temperatures but correlated with the two-pyroxene thermometer data (T_{CaM}: 894–1056 ± 25°C and T_{WES}: 897–1053 ± 15°C), except the two amphibole-rich peridotites (GN1407 and BF1411), where T_{WES} is lower than T_{BK} by more than 150°C.

We estimated the depth of origin of the xenoliths by plotting their T_{BK} equilibrium temperatures on the geotherm derived from surface heat flow data (Figure 3, Artemieva, 2009; Lenkey et al., 2002;

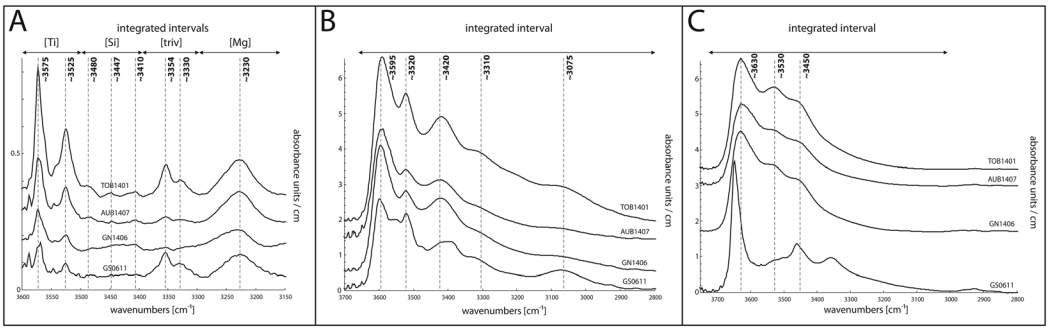

Figure 4. Average unpolarized spectra of representative (a) olivine, (b) orthopyroxene, and (c) clinopyroxene in the studied Styrian xenoliths. The spectra are normalized to 1 cm. The scale bar is equivalent of 0.5 absorbance unit.

Sachsenhofer et al., 1997). The xenoliths must have been derived from a depth between ~27 km and ~58 km, which is consistent with the recent Moho and lithosphere-asthenosphere boundary (LAB) estimations in the SB of 28 and 60–80 km, respectively (Bianchi et al., 2014; Horváth et al., 2006). Based on this depth estimation, the studied mantle xenoliths represent a comprehensive sampling of most of the lithospheric mantle column beneath the Styrian Basin. Compared to previous studies, which focused on xenoliths from Kapfenstein (Coltorti et al., 2007; Dobosi et al., 2010; Kurat et al., 1991), our samples display a wider equilibrium temperature range with several xenoliths exhibiting equilibrium temperatures (T_{BK}) below 950°C (Figure 3).

4.3. Infrared Spectroscopy of Nominally Anhydrous Minerals

Representative infrared spectra of NAMs in the studied Styrian xenoliths are presented in Figure 4. In olivines, the most intense (maximum linear absorption and integrated area) absorption bands are around 3,575 and 3,525 cm^{-1} (Figure 4). A band around 3,230 cm^{-1} is usually the second most intense one. In some xenoliths (amphibole-rich harzburgites BF1411 and GN1407; porphyroclastic lherzolites GS0610 and GN1402) this band is equally intense or more intense than the 3,575 and 3,525 cm^{-1} bands. Besides these bands, the characteristic bands at ~3,355 and 3,330 cm^{-1} were also observed in every sample. Small bands between 3,500 and 3,400 cm^{-1} are present in all studied xenoliths, except lherzolite NH0601A, but their intensity is weak, and hence, their contribution to the structural hydroxyl content of the olivines is negligible. The concentration of H_2O in olivine ranges from ~5 to 10 ppm in most studied xenoliths. In lherzolite NH0601A, water content in olivine is as low as 3 ppm, whereas in five xenoliths olivine has structurally bonded hydrogen contents higher than 10 ppm (up to 12.8 ppm in porphyroclastic lherzolite TOB1401; Table 1).

Orthopyroxenes have three strong absorption bands around 3,595, 3,520, and 3,420 cm^{-1} (Figure 4), which intensities become weaker with descending wave numbers. Weaker bands are observed around 3,310 and 3,075 cm^{-1}. A small shoulder at ~3,630 cm^{-1} is also present in most of the samples, but its contribution to the hydroxyl signal of orthopyroxenes is negligible. In the phlogopite-containing amphibole-rich harzburgite BF1411, absorption bands at ~3,710 and ~3,686 cm^{-1} were also observed. The hydroxyl content of orthopyroxenes ranges between 84 and 290 ppm.

Clinopyroxenes display three main bands, which exhibit descending intensities from ~3,630, ~3,530, to 3,450 cm^{-1} (Figure 4). The only exception is the fine-grained equigranular lherzolite GS0611, where the Ca-rich diopside (>24 wt %) has a distinct spectrum (Figure 4). This sample also exhibits three main absorption bands, but they are shifted to ~3,648, ~3,460, and ~3,357 cm^{-1}. Bands at ~3,710 and 3,686 cm^{-1} are identified in all studied clinopyroxenes, but these bands are significant only in lherzolite GN1411. The water content of clinopyroxenes ranges from 190 to 674 ppm.

The bulk "water" contents of the studied peridotite xenoliths, calculated from the hydroxyl content of the minerals and the samples' mode, are given in Table 1 in ppm wt % H_2O. In this estimation it was assumed that amphiboles contain 1.5 wt % H_2O water (Table 1). The bulk water content of the studied xenoliths ranges between 45 and 396 ppm, except for the amphibole-rich xenoliths BF1411, GN1407, and TOB1403, which show much higher water concentrations (1,374–2,395 ppm). In all xenoliths where the modal proportion of

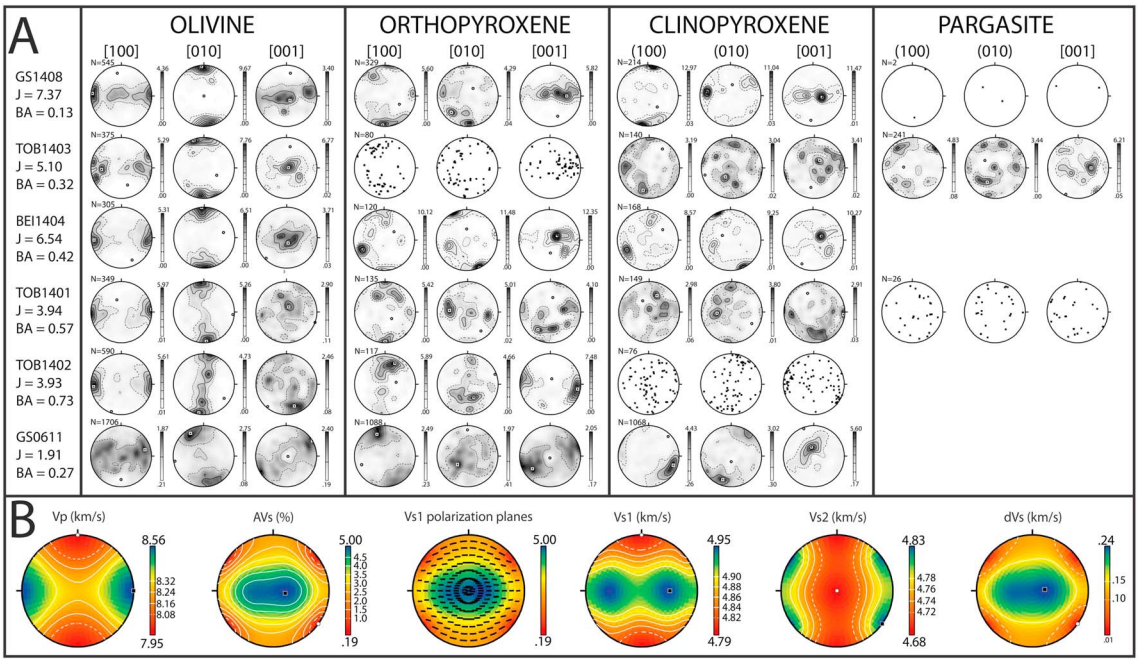

Figure 5. (a) Crystal-preferred orientations (CPOs) of olivine, orthopyroxene, clinopyroxene, and pargasite from representative Styrian xenoliths. The full data set can be found in Figure S2 in the supporting information. Pole figures are represented using one point per grain averaged orientations to avoid the overrepresentation of larger grains. All CPOs have been rotated toward [100] maxima east-west and [010] maxima north-south. *N* = is the number of measured grains. Contours at 1 multiple of uniform distribution intervals. The olivine fabric type and strength are given by the *J*-index and the by the *BA*-index, respectively. Pole figures were not contoured when less than 100 grains were measured. (b) Calculated average seismic properties of the Styrian Basin subcontinental mantle lithosphere based on the CPO and modal compositions of the studied SB xenoliths.

amphibole is higher than 5%, the H_2O content in whole rock is controlled by amphibole content. In contrast, in amphibole-poor xenoliths, the bulk water content shows positive correlation to the structurally bonded H content in pyroxenes, suggesting that pyroxenes control the water budget of these peridotite xenoliths. Strong correlation between the xenoliths water content and petrographic texture was not recognized. However, it is worth mentioning that the lowest water concentrations in orthopyroxene and clinopyroxene, below 100 and 300 ppm, respectively, are observed in coarse porphyroclastic xenoliths (Table 1).

4.4. Crystal-Preferred Orientations

Crystal-preferred orientations of olivine, orthopyroxene, clinopyroxene, and pargasite for representative samples are shown in Figure 5a. Data for all samples are presented in Figure S2 in the supporting information. Based on the *BA* indices of olivine (Table 1), the mantle xenoliths from the Styrian Basin are characterized by [010]-fiber, orthorhombic and [100]-fiber symmetries. These three olivine CPO symmetries are the most abundant in the mantle, composing >85% of the published CPO data from mantle xenoliths and massive peridotites from different geodynamical environments (Tommasi & Vauchez, 2015). In the present data set, olivine CPO transitional between the [010]-fiber and the orthorhombic types strongly predominate (26 out of 33 xenoliths) and axial [100] CPO are rare (Table 1).

In the studied SB xenoliths, which display a clear foliation, peridotites with [010]-fiber symmetry (Figure 5a) are characterized by a strong point concentration of [010] axes of olivine normal to the foliation. The [100] and [001] axes have girdle-like distributions in the plane of the foliation with weak maxima at ~90° to each other. The predominance of this symmetry type in the studied sample set (54.5%) is higher than the world average (10.1% of peridotites; Ben Ismail & Mainprice, 1998). In the SB xenoliths exhibiting orthorhombic olivine CPO symmetry, all the three major crystallographic axes show strong point like maxima (Figure 5a). In samples with a clear foliation and lineation, the [100] axes lie in the plane of the foliation parallel to the stretching lineation. The [010] axes are aligned parallel to the pole of the foliation. Accordingly, the [001] axis is concentrated in the plane of the foliation, normal to the lineation (Figure 2f/2). In the oriented samples,

which exhibit [100]-fiber symmetry (Figure 5a), the [100] axis shows a strong point concentration parallel to the lineation, whereas the [010] and [001] axes have girdle-like distributions in the plane of the foliation. These latter two symmetry types are more frequent in peridotites worldwide than in the Styrian Basin (49.5% versus 33% for the orthorhombic fabric and 23.8% versus 12.0% for the [100]-fiber symmetry, respectively; Ben Ismail & Mainprice, 1998).

Except for three xenoliths showing a [100]-fiber symmetry (harzburgite NH1403, lherzolite TOB1402, and orthorhombic lherzolite TOB1401), the [010] axes are the most concentrated, showing the highest maximum intensities on the pole figures (Figure 5). The distribution of rotation axes accommodating low-angle (2–15°) misorientations within olivine grains shows strong concentrations around the [010] and [001] axes with the former being more concentrated, except in the xenolith lherzolite TOB1402 ([100]-fiber symmetry), where [001] is more concentrated.

The *J*-index of olivine (calculated from the whole orientation data set) ranges between 2.1 and 9.7 and shows similar distribution to the global data set (Tommasi & Vauchez, 2015). The exception is the texturally unique fine-grained equigranular xenolith GS0611, which exhibits weak ($J = 1.91$), although clear CPO. The *J*-index shows a weak positive correlation with average grain size of olivine (Figure 6a), indicating that its value may be slightly overestimated in the coarsest-grained xenoliths. *BA*-index shows no correlation with fabric strength (*J*-index) similar to the report in Mainprice et al. (2014).

Orthopyroxene displays weaker, more dispersed CPO than olivine. In nearly all samples, the concentration of [001] axes of orthopyroxene are subparallel to the olivine [100] axes maximum and parallelism between olivine [010] axes and orthopyroxene [100] axes maxima were observed in 2/3 of the xenolith suite. In most samples, orthopyroxene [001] axes show the highest intensities (Figure 5a).

Clinopyroxenes have much weaker CPO than olivine and orthopyroxene, but those are usually subparallel to the orthopyroxene CPO (Figure 5a). The only exception is the fine-grained lherzolite GS0611, where all three major crystallographic axes show strong point-like maxima with clinopyroxene [100] and [001] axes distributed roughly perpendicular to those of orthopyroxene (Figure 5a). In this sample, the [001] axes of clinopyroxene are parallel to the clinopyroxene layering but normal to the orthopyroxene [001] concentration, whereas the [010] axes of clinopyroxene are perpendicular to the layering. Moreover, in this sample, clinopyroxene exhibits a stronger CPO than olivine and orthopyroxene, although it has the lowest *J*-index ($J_{cpx} = 2.95$) among the studied xenoliths. Note that *J*-index of clinopyroxene in the coarse-grained xenoliths is probably overestimated due to the lower number of clinopyroxene grains measured.

Within the spinel-pyroxene clusters, orthopyroxene and clinopyroxene have similar orientations and the pyroxene [001] and [010] axes are distributed subparallel to the [111] and [110] axes of the closest spinel grain, respectively (Figure S3 in the supporting information). This is in agreement with the topotaxial relationship of pyroxene and spinel after subsolidus garnet breakdown at high temperature (Obata & Ozawa, 2011).

Amphibole forming rims around pyroxenes and spinels shows (100), (010), and [001], which are perfectly aligned with the [100], [010], and [001] axes of pyroxenes, respectively (Figure 2f/1). Moreover, in the spinel-pyroxene clusters where amphibole completely replaced the pyroxenes, we observed the same topotaxial relationship as for pyroxene-spinel pairs in fresh spinel-pyroxene clusters (Obata & Ozawa, 2011) but with amphibole (010) and [001] distributed parallel to the spinel [110] and [111], respectively (Figure 2f/1).

4.5. Seismic Properties

The three-dimensional distribution of seismic properties was calculated based on the CPO and modal abundance of olivine, orthopyroxene, and clinopyroxene of the studied xenoliths (Mainprice, 1990). The average seismic properties of the SCLM beneath the Styrian Basin were estimated by averaging the calculated elastic tensors of each xenolith. The foliation and lineation were assumed to have a constant orientation in all xenoliths; therefore, we used the rotated CPO data sets (maximum of [100] to the east-west, maximum of [010] to the north-south). Consequently, the average value is a maximum estimate of the seismic properties of the studied xenoliths. For olivine, orthopyroxene, and clinopyroxene, the single crystal elastic tensors of Abramson et al. (1997), Jackson et al. (2007), and Isaak et al. (2006) at ambient pressure were used, respectively. Although amphibole is a significant constituent of some samples, its CPO is always very weak; by

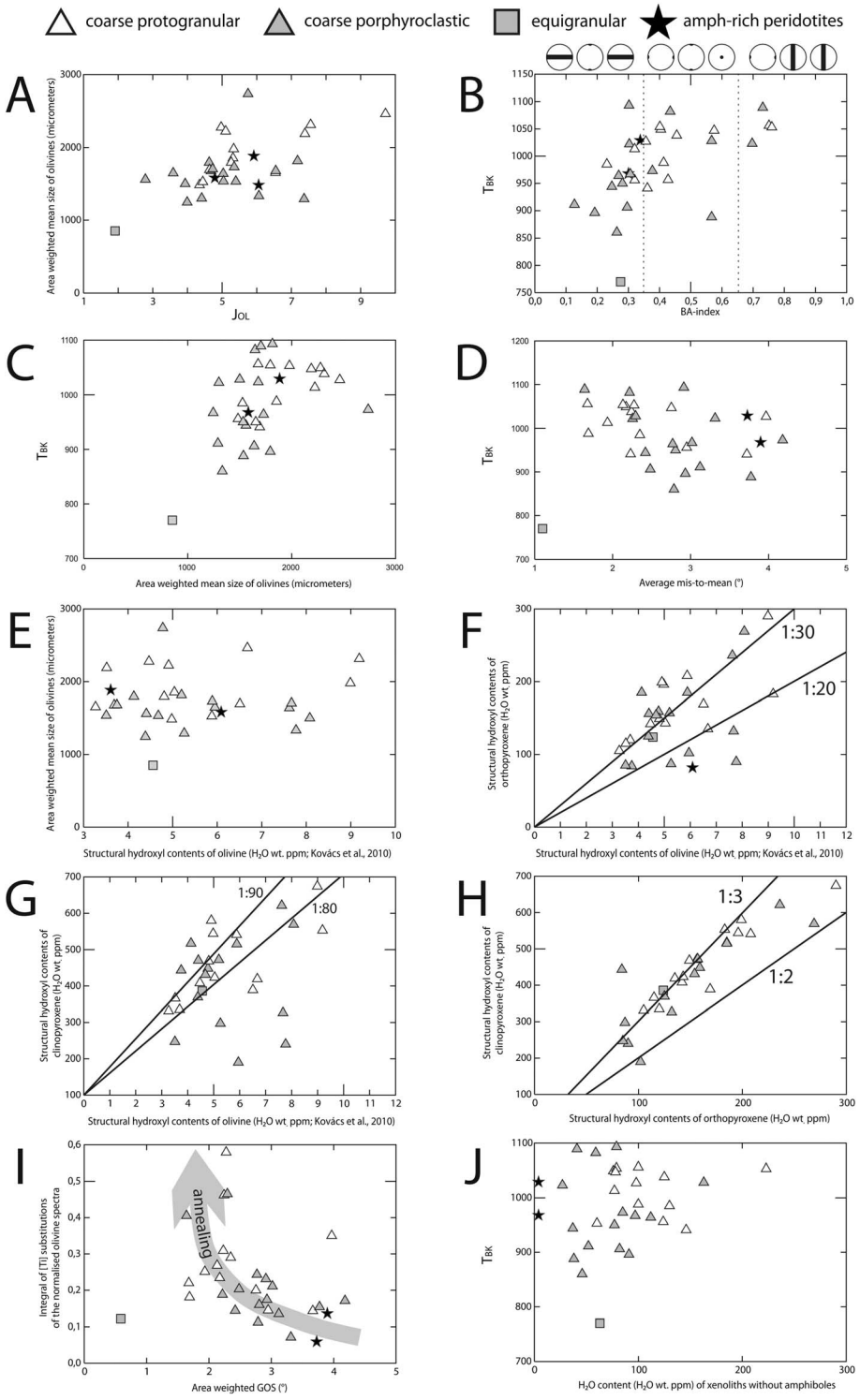

Figure 6. (a–h) Scatterplots of EBSD and FTIR data.

consequence its main impact will be to slightly reduce the anisotropy. It was omitted in the calculations. A Voigt-Reuss-Hill averaging was applied in all calculations.

The 3-D distribution of the average seismic properties, shown in Figure 5b, is fairly similar to those of individual peridotite xenoliths. In average, the fastest *P* wave (8.56 km/s) direction is aligned with olivine [100] axis

maxima, which corresponds to the lineation in most samples. The *P* wave propagation is the slowest (7.95 km/s) normal to the foliation. The *S*1 wave polarization planes contain systematically the olivine [100] axis maximum, and therefore, the measured *S*1 polarization direction will be parallel to the projection of the lineation, which marks the fossil mantle flow direction, on the surface. The *S* wave splitting is minimum or absent for waves propagating at ~45° to the lineation in the *XZ* plane, and it is the highest at high angle (<45°) to the lineation in the foliation plane.

The most significant variation among xenoliths was observed in the intensity of the anisotropy. The maximum values range between 3.2 and 12% for *P* wave propagation anisotropy and between 2.4 and 7.8% for *S* wave polarization anisotropy (Table 1), being 7.4 and 5% on average, respectively. As usual a positive correlation was observed between the fabric strength of olivine (*J*-index) or the olivine modal content and the *P* and *S* wave anisotropies (Table 1). Weak positive correlation between the seismic anisotropy and the average M2M was also observed. No correlation was observed between the seismic anisotropy intensity and the olivine CPO symmetry.

5. Discussion

5.1. Hydration State of the Styrian Lithospheric Mantle

5.1.1. Incorporation of Hydrogen in Nominally Anhydrous Minerals of the Styrian Basin Mantle Xenoliths

The observed absorption bands related to structural hydroxyl substitutions in nominally anhydrous minerals (NAMs) of the Styrian xenoliths (Figure 4 and Table S1 in the supporting information) agree with the published literature data. In olivine we observed the four most common substitution of H (e.g., Balan et al., 2011; Berry et al., 2005; Kovács et al., 2010) including (1) Ti-clinohumite-like point defects [Ti] (bands around 3,525 and 3,575 cm^{-1}), (2) tetrahedral Si vacancies [Si] (3,505–3,405 cm^{-1}), (3) trivalent cations compensated by H bound to oxygen in the neighboring octahedron [triv] (3,355–3,330 cm^{-1}), and (4) octahedral vacancies [Mg] (around 3,230 and 3,180 cm^{-1}). The [Ti] and [Mg] substitutions correspond to the most intense bands, which are present in all but two xenoliths (NH0601A and NH1408 coarse porphyroclastic lherzolites) (Figure 4), whereas [Si] substitution seems to be negligible. This latter observation is consistent with the assumption that the lithospheric mantle, represented by the presently studied xenoliths, is enstatite buffered, what hinders the generation of Si vacancies. The structural hydroxyl contents of olivine (Table 1) range between 3 and 13 using the Bell et al. (2003) calibration or 3 and 9 ppm wt. H_2O using the Kovács et al. (2010) calibration.

In orthopyroxenes, the observed main absorption bands around 3,595, 3,520, and 3,420 cm^{-1} and weaker ones around 3,310 and 3,075 cm^{-1} (Figure 4) are typical for mantle-derived orthopyroxenes (e.g., Bonadiman et al., 2009; Gavrilenko, 2008; Stalder & Ludwig, 2007). The small shoulder at ~3,630 cm^{-1} may originate from clinopyroxene lamellae. In the phlogopite-bearing amphibole-rich harzburgite BF1411, absorption bands of pargasite were also observed at ~3,710 and ~3,686 cm^{-1} in addition to those of orthopyroxene (Della Ventura et al., 2007). The structural hydroxyl content in orthopyroxenes ranges from 84 to 290 H_2O wt ppm (Table 1).

In clinopyroxenes, the observed bands at ~3,630, ~3,530 to 3,450 cm^{-1} are quite common in mantle peridotites (e.g., Bonadiman et al., 2009; Pintér et al., 2015; Stalder & Ludwig, 2007). We also detected the bands of pargasitic amphibole at ~3,710 and 3,686 cm^{-1} in all studied clinopyroxenes (Della Ventura et al., 2007). These latter bands become significant only in lherzolite GN1411, where they lead to overestimation of the H content of the clinopyroxene. In the other xenoliths, the contribution of amphibole to the estimated structural hydroxyl content of clinopyroxenes is negligible. In these samples, the structurally bonded hydroxyl content in the clinopyroxenes ranges from 190 to 674 H_2O wt ppm (Table 1).

5.1.2. Preservation and Concentration Levels of Hydrogen in the Styrian Xenoliths

Based on the lack of correlation between grain size and structural hydroxyl content in olivine (Figure 6e), the lack of diffusion profiles in olivines, and the correlation in most samples between H_2O content of olivine and pyroxenes (Figures 6f and 6g), we assume that the amount of hydrogen loss in the Styrian xenoliths was negligible. Therefore, the H_2O content in the xenoliths may represent the original H_2O content of the SCLM beneath the region. This interpretation is also supported by the presence of absorption bands related to hydrated octahedral vacancies ([Mg]). Hydrous defects related to octahedral vacancies diffuse an order of

magnitude faster than Ti-related substitutions (Padrón-Navarta et al., 2014). Thus, a strong signal in the [Mg] bands imply that out-diffusion of structural hydroxyl from olivines was very limited in the Styrian Basin. On the other hand, the fast diffusion of hydrated octahedral vacancies might explain the absence or the negligible intensity of [Mg] absorption bands in most olivines from spinel facies peridotite xenoliths from other localities (e.g., Demouchy et al., 2015; Denis et al., 2015; Grant et al., 2007; Schmadicke et al., 2013; Yu et al., 2011). In the studied Styrian xenoliths the bands of [Mg] are intense (Figure 4) in all but two samples (NH0601A and NH1408). The presence of [Mg] hydroxyl defects could also be explained by high activity of water (Tollan et al., 2017). Schmadicke et al. (2013) reported similar results, where structural hydroxyl content of an olivine from the Styrian Basin (Kapfenstein) was estimated to be 16 ppm H_2O (with the method of Bell et al., 2003), without any signs of hydrogen loss (based on Ti concentrations in olivine and on the intensity of hydroxyl bands in Ti-related substitutions).

The partition coefficient of H between the clinopyroxene and orthopyroxene ($D_{H_2O}^{cpx/opx}$) is close to 3, tending toward 2 at higher concentrations (Figure 6h; $(D_{H_2O}^{cpx/opx})_{avg} = 2.86 \pm 0.57$), which is slightly higher than the generally observed values (2.3 ± 0.5: Pintér et al., 2015, and references therein; 2.1: Demouchy & Bolfan-Casanova, 2016; ~2: Hao et al., 2016; Xia et al., 2010). This narrow range of partition coefficient of H between the two pyroxenes corresponds to near-equilibrium conditions, implying that no significant hydrogen loss affected the pyroxenes in the Styrian xenoliths.

Our results agree with previous studies, which propose that pyroxenes usually preserve their original structural hydroxyl contents of their source mantle region (e.g., Denis et al., 2013; Hao et al., 2014, 2016; Li et al., 2015; Pintér et al., 2015; Xia et al., 2010). Our data, therefore, suggest that the upper mantle-derived Styrian mantle xenoliths probed the original structural hydroxyl content of the SCLM, which was not exposed to diffusional loss of hydrogen during the entrainment of the xenoliths in the host basalt.

The Styrian mantle is considered to be water rich, compared to other spinel facies peridotite xenoliths from off-cratonic settings (Demouchy & Bolfan-Casanova, 2016, and references therein). In olivine, the concentration of structural hydroxyl was over the detection limit in every sample and the maximum is well above 10 ppm (with the calibration factor of Bell et al., 2003). These high concentrations may seem to be exceptional in a young, extensional basin, where the hot SCLM is composed of spinel peridotites. A detailed study on nominally anhydrous minerals in xenoliths from the Persani Mountains (Falus et al., 2008) reported similarly high concentrations of hydroxyl in orthopyroxene, clinopyroxene, and olivine (100–300 ppm, 200–650 ppm, and 2–15 ppm, respectively) from highly deformed porphyroclastic and mylonitic peridotites. They suggested local hydration in the lithospheric mantle, opposed to an extensive enrichment in volatiles due to pervasive melt/fluid migration, beneath the Persani Mountains, which corresponds to a supra subduction setting. High concentrations were also reported in xenoliths from different geodynamic environments where the SCLM went through refertilization via metasomatism such as the North China Craton (Yang et al., 2008), the South China Block (Yu et al., 2011), the Ontong Java Plateau (Demouchy et al., 2015), and from the East African Rift System (Baptiste et al., 2015).

The water content of the bulk peridotites is controlled by orthopyroxene and clinopyroxene, except in amphibole-rich samples, where postkinematic, late-stage amphibole formation enriched the samples in water. Equilibrium temperature can have a huge effect on the distribution of hydrogen in the mantle peridotites since pargasite, which is the main host of hydroxyl, is stable only under ~1100°C and ~3 GPa (Green et al., 2010; Kovács, Green, et al., 2012; Kovács et al. 2017). Beyond the stability of pargasite, the hydrogen resides mainly in the NAMs and in a free fluid/melt phase may be present. All studied samples equilibrated below 1100°C (Figure 3), and most of them contain secondary amphibole (Table 1), but we could not observe a correlation between the equilibrium temperature of the samples and their structural hydroxyl content. If the water content of late-stage amphiboles is not considered when calculating the whole-rock water contents, pyroxenes are still the main host of the structurally bond hydroxyl in the mantle beneath the Styrian Basin. The three amphibole-rich peridotites (Figure 2d and Table 1) do not show significantly different amount of structural hydroxyl in olivine and pyroxenes compared to the rest of the xenolith suite (Table 1). Without amphiboles, the coarse-grained protogranular xenoliths and those with higher equilibrium temperature (>950°C) tend therefore to have higher bulk water contents (Table 1 and Figure 6j). This observation agrees with the global phenomenon that the hydroxyl concentrations in the NAMs of peridotite xenoliths increase as a function of depth, in both spinel and garnet facies (see the review of Demouchy & Bolfan-Casanova, 2016).

5.2. Deformation and Annealing of the Styrian Mantle Lithosphere

5.2.1. Microstructure, Mechanisms, and Conditions of the Deformation

Based on the petrographic observation indicating that all xenoliths were equilibrated in the spinel facies, the calculated equilibrium temperatures and the proposed geotherm for this region (Table 1 and Figures 2 and 5a), we conclude that the studied xenoliths have been derived from a ~30 km thick domain (approximately from 30 to 60 km depth) of the subcontinental lithospheric mantle (Figure 3). Hence, analysis of the xenolith suite implies that the shallow lithospheric mantle beneath the Styrian Basin may be essentially dominated by protogranular and porphyroclastic lherzolites (Table 1). The majority of these xenoliths are coarse grained (Figures 2 and 6a: grains are several millimeters in dimension) and contain olivines with straight grain boundaries meeting in 120° triple junctions (Figure 2), suggesting textural equilibrium. The limited textural evidence for intragranular deformation, such as the general lack of subgrain boundaries and rare undulose extinction, particularly in the protogranular textures, and the low degree of intragranular misorientations (average M2M values ranging between 2 and 4°, Table 1), suggests that textural equilibrium was achieved by annealing phenomena. Despite the dominantly annealed textures in the xenolith suite, clear olivine and orthopyroxene CPO are observed in all xenoliths, except the equigranular one (GS0611), and CPO strength are moderate to strong (*J*-index = 2–9, Table 1 and Figure 2a). In addition, evidence for plastic deformation, like kinks, subgrains, elongated pyroxene grains/clusters, and holly-leaf spinels, is locally preserved, particularly in the porphyroclastic xenoliths (Figures 2b and 2c). We interpret that these microsctructures and CPO as evidence for plastic deformation, accommodated by dislocation creep, affected the SCLM beneath the Styrian Basin prior to annealing. These petrographic features suggest that the deformation of the studied xenoliths occurred in the shallow lithospheric mantle at high temperature (>1000°C) and relatively dry conditions in the dislocation creep regime (Carter & Avé Lallemant, 1970). The evidence for deformation of pyroxene-spinel clusters (Figure 2f) after subsolidus breakdown of garnet (Falus et al., 2000) confirms that the observed plastic deformation of the lithospheric mantle took place in the spinel stability field. This deformation was followed by static recrystallization (=annealing). The lack of correlation between the equilibrium temperatures and average grain size and M2M values (Figures 6c and 6d) implies that annealing affected the whole lithospheric mantle, irrespectively from depth.

In the xenoliths where a foliation and a lineation can be observed, the [100] axes of olivines and [001] axes of orthopyroxenes are parallel to the lineation in the foliation plane. Clinopyroxenes are more dispersed, but their CPOs are similar to those of the orthopyroxenes, except in the fine-grained equigranular lherzolite GS0611 (discussed later) (Figure 2e). The subparallel distribution of olivine [100] axes and the [001] axes of orthopyroxene and clinopyroxene (Figure 5) suggest coherent deformation of the main rock forming silicate minerals. Note that this internal correlation between the CPO of olivine and pyroxenes is also observed in those xenoliths, where structural elements are not visible in the rock. The olivine and enstatite CPO are slightly oblique to each other (<20°). This obliquity is often observed in mantle rocks, and it is generally explained by lower strains accommodated by the harder enstatite grains (Tommasi et al., 2006).

Based on the alignment of the dominant slip direction with the maximum stretching direction in simple shear deformation (e.g., Tommasi et al., 1999; Zhang & Karato, 1995), we assume a dominant [100] slip direction in olivine and [001] slip direction in the pyroxenes of the SB xenoliths. This is further supported by the preserved subgrain walls in olivine that typically form perpendicular to the [100] crystallographic axes, irrespective to the CPO symmetry type (Figure 2f) and by the low angle intragranular misorientations (2–15°) that record rotations dominantly around [010] in orthopyroxene and around <0vw> in olivine. The observed orthopyroxene CPO is compatible with dominant slip in the [001] direction on the (100) plane. Dominant activation of [100] glide in olivine is favored under low pressure (Couvy et al., 2004; Mainprice et al., 2005; Raterron et al., 2004). Experimental data also imply that [100] glide is favored at low to moderate (2–15 ppm) structural hydroxyl contents (Jung & Karato, 2001; Karato et al., 2008). These are in agreement with the observed structural hydroxyl contents and with the suggested deformation in the spinel peridotite facies.

In most Styrian Basin xenoliths, olivine exhibits dominantly a transitional CPO symmetry between [010]-fiber and orthorhombic; only a few xenoliths show [100]-fiber CPO symmetry. According to experiments, numerical models and theoretical considerations (e.g., Hansen et al., 2014; Tommasi et al., 2000, 1999), orthorhombic and axial [100] olivine fabric types can be produced by deformation in simple shear with dominant activation of (010)[100] or {0kl}[100] slip systems, respectively. In contrast, activation of the same slip systems in transpression produces axial [010] olivine fabrics (Tommasi et al., 1999). [010]-fiber olivine CPO patterns are

common in nature. They were described in the Ronda and Lherz peridotite massifs (e.g., Le Roux et al., 2007; Vauchez & Garrido, 2001), in the Oman ophiolite (Higgie & Tommasi, 2012), in cratonic xenoliths (Baptiste et al., 2012; Vauchez et al., 2005) and off-cratonic xenoliths (e.g., Baptiste et al., 2015; Bascou et al., 2008; Kourim et al., 2015; Tommasi & Ishikawa, 2014; Zaffarana et al., 2014). However, these studies proposed that this CPO symmetry is not only produced in transpressional deformation regimes (Tommasi et al., 1999, 2000), but that it may also form in response to concomitant activation of [001] and [100] glide (e.g., Demouchy et al., 2014, 2013; Vauchez et al., 2005), or by deformation in the presence of melt with high melt/rock ratio (Higgie & Tommasi, 2012, 2014). Annealing or recrystallization by subgrain rotation can also cause the dispersion of [100] (Falus et al., 2011). This is consistent with the observed low-angle misorientations that are mainly accommodated by rotations around $<0vw>$, that is, around directions normal to [100]. It is also consistent with the predominance of [010]-fiber patterns in the coarse-porphyroclastic xenoliths, whereas coarse protogranular xenoliths show dominantly orthorhombic patterns (Figure 6b). The observed misorientation axes in olivine also indicate subgrains composed by dislocations of the (001)[100], (010)[100], or (100)[001] systems. Yet the latter is not consistent with the dominant orientation of the subgrains parallel to (100). The lack of evidence for activation of [001] glide favors the transpression hypothesis to explain the [010]-fiber olivine CPO patterns. Transpressional deformation should also disperse the [001] axes of pyroxenes in the foliation plane (Baptiste et al., 2012; Bascou et al., 2008; Tommasi et al., 2006; Vauchez & Garrido, 2001). This dispersion is observed in most of the studied SB xenoliths characterized by $BA < 0.40$ mainly in the case of orthopyroxenes, but in some xenoliths clinopyroxenes [001] are also dispersed (e.g., GS1408 and NH1408; Figures 5a and S2 in the supporting information). Independently of their microstructure, xenoliths equilibrated at higher temperatures display more variable olivine CPO patterns; they are the only ones to show [100]-fiber patterns (Figure 6b). This is consistent with the observations of Falus et al. (2011) that grain growth, favored at higher temperatures (>1000°C; Falus et al., 2008), results in less dispersion of the CPO and, in particular, of the [100] axis of olivine than subgrain rotation recrystallization. It is worth to mention that olivines in highly annealed xenoliths from intracratonic settings (Siberia, Tommasi et al., 2008; Kaapvaal, Baptiste et al., 2012) also show [010]-fiber CPO. Data in the literature on the effect of static annealing on olivine CPO are scarce. Observations in the Ronda peridotites imply that static annealing does not significantly change the CPO (Vauchez & Garrido, 2001), whereas the previously cited data on xenoliths suggest that it may result in dispersion of the olivine CPO. To conclude, deformation in a transpressional setting seems, therefore, the most plausible scenario to produce the dominant transitional orthorhombic—[010]-fiber CPO symmetry in olivine and the dispersed [001] axes of pyroxenes in the foliation plane.

The amphibole overgrowths on pyroxenes and the absence of microstructural evidence of intracrystalline deformation in amphiboles suggest that their CPO is inherited, resulting from topotaxial growth and not formed by dislocation creep. Based on these observations, we explain the formation of amphiboles as rims on the pyroxenes and spinels (Figure 2f/1) as a postkinematic process resulting from reactions between the peridotites and migrating hydrous melts (e.g., Kaczmarek & Tommasi, 2011; Kourim et al., 2015). There is no evidence for presence of melt during the deformation, except in the case of the equigranular xenolith GS0611 (Figure 2e) (discussed below).

The fine-grained equigranular lherzolite GS0611 differs from the other studied xenoliths in this suite by its unique texture, low equilibrium temperature (T_{BK} = 770°C), very weak CPO of olivine (J_{OL} = 1.91, Table 1), and clear CPO of clinopyroxenes (Figure 5a). Recrystallization under low-temperature and high strain rate can promote the development of fine-grained peridotites with low fabric strengths (Falus et al., 2011). Such deformation is usually associated with localized shear zones (e.g., Vauchez et al., 2012) that can provide paths to fluid flow and/or melt channeling (e.g., Hidas, Tommasi, et al., 2016; Kourim et al., 2015; Kruckenberg et al., 2013; Tommasi et al., 1994). Deformation in the presence of melt often results in weak CPO of olivine with a [010]-fiber symmetry (e.g., Higgie & Tommasi, 2012; Kourim et al., 2015; Kruckenberg et al., 2013; Le Roux et al., 2008; Soustelle et al., 2009). The layering marked by clinopyroxene enrichment and interstitial shapes of clinopyroxene (Figure 2e) suggest late clinopyroxene addition. Yet the clinopyroxene CPO in this sample is stronger than the olivine and orthopyroxene ones. The orientation of [001] axes parallel to the bands trend, but normal to the orthopyroxene [001] maximum, and of [010] axes normal to it might be explained by oriented crystallization from a melt under a deviatoric stress state controlled by the opening of the pyroxene vein (e.g., Zaffarana et al., 2014). Peridotite xenoliths with similar textures were reported by Embey-Isztin et al. (2014) in the nearby Bakony-Balaton Highland Volcanic Field within the CPR. These authors proposed that

these xenoliths were formed due to "percolative fractional crystallization" with high melt/rock ratios at the lithosphere-asthenosphere boundary. Based on our results, we suggest that the fine-grained equigranular lherzolite GS0611 records deformation in presence of melts, probably in a localized shear zone.

5.2.2. Fluid-Enhanced Annealing in the Styrian Basin SCLM Contrary to the Central CPR

The very low density of intragranular deformation microstructures in olivine (e.g., subgrain boundaries, neoblasts, and undulose extinction), despite the well-developed CPO of olivine and pyroxenes (Figures 2 and 5), indicates that annealing phenomena are likely one of the latest events recorded in the Styrian Basin xenoliths. Considering that the degree of annealing in the studied xenolith suite shows no correlation with equilibrium temperature, texture type, CPO strength, or symmetry (Table 1), we conclude that this young event affected the entire shallow SCLM beneath the Styrian Basin. Based on the petrographic features, structural data and hydroxyl contents (Tables 1 and S2), we propose that annealing in the studied xenoliths could have been enhanced by fluid (including melt) migration. This fluid migration may have resulted in fluid-assisted annealing of the xenoliths. The elevated structural hydroxyl content in Ti substitution sites of annealed olivines compared to the more deformed ones (Figure 6i) supports fluid-aided annealing in the SCLM of the Styrian Basin. This is in agreement with experimental results showing that under water-undersaturated conditions the Ti-related H defect is the most stable one and the first to be hydrated (Faul et al., 2016; Tollan et al., 2017). Similar findings on metasomatism related annealing were reported previously from the Hoggar swell, Algeria (Kourim et al., 2015).

According to Falus et al. (2000), the garnet breakdown can be associated with the Miocene extension of the Pannonian Basin, during which the lithospheric mantle went through significant thinning process (Sachsenhofer et al., 1997). Symplectites after garnet breakdown during the Miocene extension were found both in spinel peridotite (Falus et al., 2007) and in lower crustal granulite xenoliths (Dégi et al., 2009) from the Little Hungarian Plain Volcanic Field and Bakony-Balaton Highland Volcanic Field, respectively (Figure 1a). However, symplectites in the LHPVF and BBHVF are texturally not as well equilibrated as those observed in the present study. We suggest that unlike the SCLM underneath the central part of the CPR, the SCLM beneath the Styrian Basin suffered rather extensive fluid migration. The presence of fluids might have caused also the coarsening of the originally fine grained symplectites (former garnets) into coarse-grained spinel-pyroxene clusters (Figures 2f and S3 in the supporting information).

As discussed in the previous section, olivine CPO with [100]-fiber symmetries are only observed among the xenoliths equilibrated at higher temperatures ($T_{BK} > 1000$°C) and axial [010] symmetries predominate among those xenoliths equilibrated at lower temperatures ($T_{BK} < 1000$°C; Figure 6a). A connection between CPO symmetry and equilibrium temperature was also observed in xenoliths from the center of the Pannonian Basin (Little Hungarian Plain and Bakony-Balaton Highland; Kovács, Falus, et al., 2012). Low-temperature (875–960°C) fine-grained xenoliths exhibit mainly [010]-fiber symmetry, whereas high-temperature (980–1160°C) coarse-grained xenoliths have orthorhombic textures. However, despite the proximity of the BBHVF to the Styrian Basin (~150 km) and the similar change in the dominant CPO symmetry with equilibrium temperature, the microstructures and hydration state in the lithospheric mantle under the two volcanic fields are different, pointing to different evolutions of the SCLM. The main differences between the Styrian Basin relative to the central parts of the Pannonian Basin are the well-annealed microstructure, the coarser grain sizes, the frequent amphibole, and the slightly lower equilibrium temperatures (~50°C). Amphiboles (or traces of amphibole in form of melt pockets) in xenoliths from the Bakony-Balaton Highland Volcanic Field are rare (e.g., Bali et al., 2002; Downes et al., 1992; Embey-Isztin et al., 1989) and mainly appear in equigranular xenoliths (Embey-Isztin, 1984; Hidas et al., 2010). Although an asthenospheric origin of the high-temperature (>1000°C) xenoliths with orthorhombic and [100]-fiber symmetries, similar to those proposed in the central part of the Pannonian Basin cannot be excluded, such xenoliths are less abundant in the Styrian Basin xenolith suite. The different evolution of the SCLM with less developed annealing in the central CPR is also supported by the predominance of deformation textures (e.g., Downes et al., 1992; Embey-Isztin et al., 2001; Hidas et al., 2007; Szabó et al., 2004) as well as the scarcity of hydrous coarse-grained textures in mantle xenoliths from the Bakony-Balaton Highland and Little Hungarian Plain Volcanic Fields (Figure 1).

5.3. Seismic Anisotropy and Estimation of the Thickness of the Anisotropic Layer

Although the studied mantle section from the Styrian Basin shows widespread annealing, the xenoliths still exhibit strong to moderate olivine CPO and, thus, seismic anisotropy (Table 1 and Figure 5b). We estimated

the thickness of the anisotropic layer that could produce the observed shear wave splitting delay times using the average seismic properties of the SB xenoliths (e.g., Ben-Ismail et al., 2001; Klébesz et al., 2015; Kovács, Falus, et al., 2012; Pera et al., 2003). As a reference we used the data measured at the seismic station Arzberg, ARSA (dt = 1.27 s; Qorbani et al., 2015), which is situated ~50 km northwest from the center of the studied area. Our calculated anisotropic thickness values range from ~150 to 3,200 km. In our calculations we ignored the potential effect of crustal anisotropy (maximum 0.1–0.2 s/10 km; Barruol & Mainprice, 1993). We considered five end-member orientations of the foliation and lineation in the SCLM (e.g., Baptiste & Tommasi, 2014; Tommasi et al., 2016): 1. horizontal foliation and lineation, 2. vertical foliation and horizontal lineation, 3. vertical foliation and lineation, 4. 45° dipping foliation and lineation, and 5. 45° dipping foliation and horizontal lineation. For cases 1 to 5, the *S* wave polarization anisotropies are 2.25, 5.0, 2.75, 0.19, and 4.0% and considering an average S wave velocity of 4.81 km/s, the calculated thickness of the anisotropic layer is 272, 122, 222, 3,217, and 153 km for cases 1–5, respectively. For a transpressional deformation, we expect a vertical foliation and horizontal lineation (case #2: 122 km). However, independently from the suggested orientation of the foliation and lineation, the calculated thicknesses are much larger than the lithospheric mantle thicknesses estimated from integrated seismic and gravity data (30–50 km: Bianchi et al., 2014; Grad & Tiira, 2009; ~70 km: Horváth et al., 2006). This indicates that at least ~100 km of anisotropic sublithospheric mantle with a consistent fabric is needed to produce the observed shear wave splitting delay times. Our calculations show that the SCLM is more anisotropic than the world average (Ben Ismail & Mainprice, 1998), but the main source of the observed *S* wave splitting cannot be the SCLM. For the 50 km thick SCLM inferred from tomographic data beneath the Styrian Basin (Bianchi et al., 2014; Horváth et al., 2006), a vertical foliation and horizontal lineation (case #2) and the average seismic properties of the studied SB xenoliths will produce 0.52 s of seismic delay time. These conclusions agree with previous interpretations by Qorbani et al. (2015), who estimated the thickness of the anisotropic layer beneath the vicinity of the Styrian Basin to be ~200 km, based on published average seismic properties of mantle peridotites (Barruol et al., 2011; Ben Ismail & Mainprice, 1998; Mainprice et al., 2000). They concluded therefore that the anisotropy signal beneath required a significant contribution from a sublithospheric layer and attributed the fast NW-SE orientation of the fast polarization at the Arzberg station (ARSA, Qorbani et al., 2015) an asthenospheric mantle flow above the detached Penninic slab under the Eastern Alps (Qorbani et al., 2015). Shear wave splitting analyses from the central part of the CPR revealed similar NW-SE fast polarization directions (Qorbani et al., 2015, 2016); the uniformity of the *SKS* splitting data across the CPR was interpreted as further evidence for an asthenospheric origin of the signal, since it contrasts with the complex crustal structure in the region. Qorbani et al. (2016) suggested that this upper mantle deformation might result from compressional tectonics caused by the collision of the Adriatic microplate and the European platform.

5.4. Geodynamic Implications

Despite a similar variation with depth of olivine CPO symmetry and microstructures, the evolution of the SCLM in the Styrian Basin is probably quite different from that in central part of CPR (see section 5.2.2). This variation can be attributed to their different position relatively to the asthenosphere upwelling generated by extension in the CPR system during the Miocene. The Styrian Basin is situated on the edge of the proposed mantle dome. Hence, the rate of the extension during the Miocene was not as extreme in the Styrian Basin (subcrustal stretching factor is ~1.6; Sachsenhofer et al., 1997) as in the central part (4–8; LHPVF and BBHVF; Figure 1; Huismans et al., 2001) of the CPR. Therefore, accretion (by cooling) of significant amount of juvenile lithosphere after the extension is not likely beneath the Styrian Basin as opposed to the central CPR (Kovács, Falus, et al., 2012).

The most recent event in the evolution of the SCLM under the Styrian Basin was the annealing. We suggest that the extensive annealing of the lithospheric mantle beneath the SBVF was enhanced by H_2O-rich fluid/melt migration events. The evidence for recent fluid/melt migrations in the lithosphere is the subduction related intermediate (~17 Ma) and postextensional (<7 Ma) alkali basalt magmatism in the Styrian Basin (Figure 1b). Teleseismic tomographic images show a cold, fast anomaly of a downwelling body beneath the Styrian Basin, which originates from the Eastern Alps and extends to the transition zone in the middle of the Pannonian Basin (Dando et al., 2011; Lippitsch, 2003; Mitterbauer et al., 2011) (Figure 1c). This structure was interpreted as a detached subducted slab, probably remnant of the Penninic slab, which subducted actively until the late Eocene (Brückl, 2011; Mitterbauer et al., 2011; Qorbani et al., 2015). Intermediate magmas (Figure 1b) erupted and intruded into the crust during the early and middle Miocene times in the Styrian

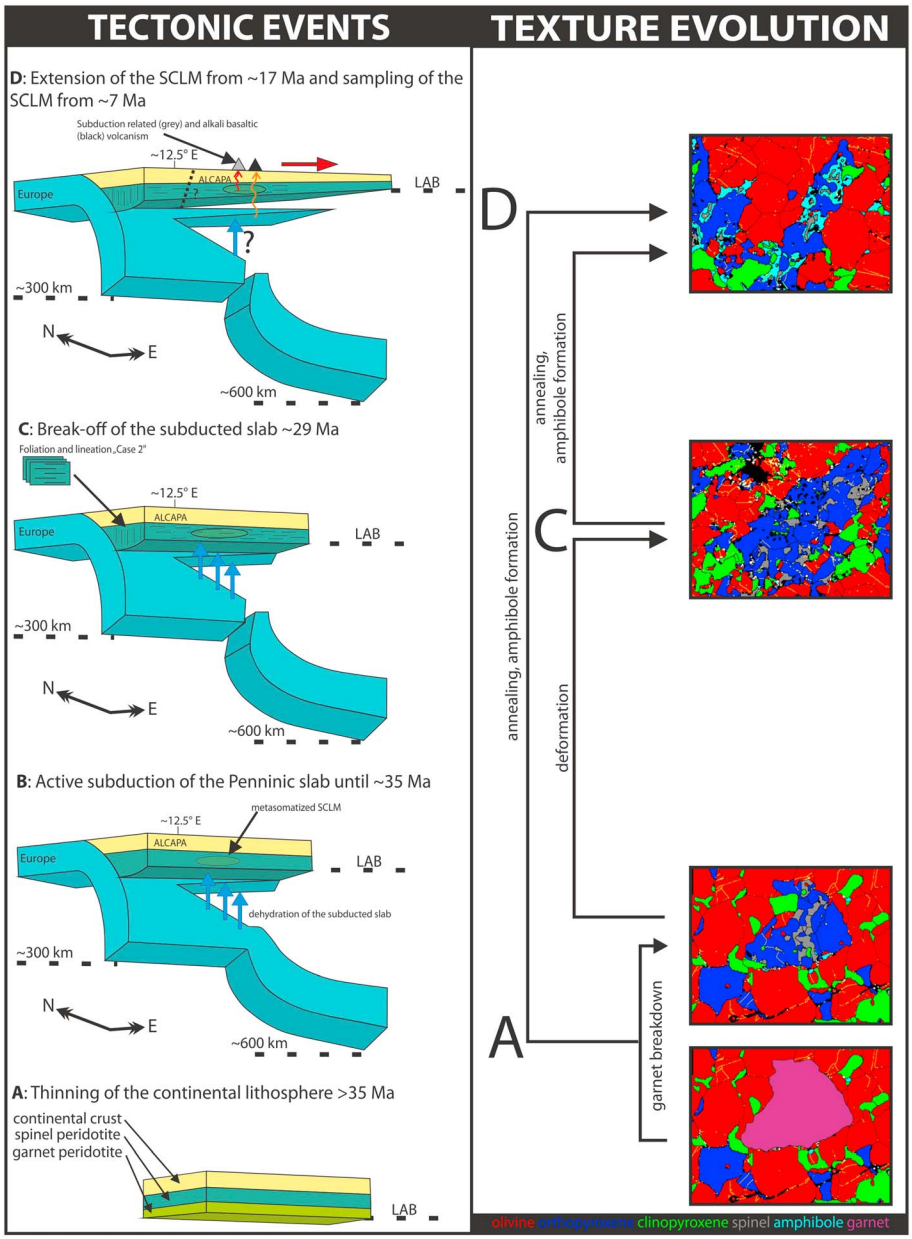

Figure 7. Tentative model of the evolution of the SCLM under the Styrian Basin, based on the slab geometry of Qorbani et al. (2015). (a) Thinning of the continental lithosphere, older than 35 Ma pre-Alpine event. Subsolidus breakdown of garnets, formation of spinel-pyroxene clusters. (b) Active subduction of the Penninic slab until ~35 Ma (late Eocene). The onset of fluid/melt migration in the SCLM, caused by the dehydrating subducted Penninic slab. (c) Slab breakoff, initiation of transpressional deformational regime around 29 Ma (Oligocene). Development of transitional orthorhombic—[010]-fiber CPO symmetries, foliation, and porphyroclastic textures. (d) Melting of the metasomatized SCLM due to the Miocene extrusion of the ALCAPA and extension of the Pannonian Basin. This initiates the subduction-related volcanism in the SB from ~17 Ma (middle Miocene). As a final step, sampling of the SCLM by postextensional alkaline basalts from ~7 Ma (late Miocene). Fluid-enhanced annealing and pervasive amphibole formation in the peridotites. The phase maps of the shown xenoliths are 1 cm wide.

Basin ~15 Ma ago (Harangi, 2001; Harangi et al., 1995). These magmas are thought to be derived from a lithospheric mantle, which was metasomatized by slab-derived hydrous fluids, and melted due to decompression caused by the Miocene extension (Harangi et al., 1995). The source of the fluid was suggested to be the late Eocene Penninic subduction. However, the hydrated mantle could also be an inherited signature of a previous, older subduction, which affected the former mantle wedge since

the SCLM — where the studied xenoliths originate — can preserve the signs of former subductions as metasomatic alterations (e.g., Kovács & Szabó, 2008). This mantle wedge scenario is in agreement with studies on amphiboles in peridotite xenoliths from Kapfenstein (Figure 1b), which revealed that alkaline mafic (Coltorti et al., 2007; Vaselli et al., 1996), and subduction-related "proto-adakite" melts (Coltorti et al., 2007), besides H_2O-rich fluids (Kurat et al., 1980; Vaselli et al., 1996), could have metasomatized the SCLM under the Styrian Basin. The source of the high structural hydroxyl contents in the NAMs of the xenoliths (Figures 4 and 1 and S2) could be also a subducted slab provided high H_2O activity environment in the SCLM of the Styrian Basin above the subducted slab (Figure 7). Rehydration of the lithospheric mantle by fluids released from a subducted slab was previously used as an explanation in the case of the North China Craton (Yang et al., 2008), the Colorado Plateau (Bell & Rossman, 1992; Li et al., 2008), and the Persani Mountains (Falus et al., 2008). On the other hand, based on a global data compilation, Demouchy and Bolfan-Casanova (2016) argued that there is no extra amount of structural hydroxyl in NAMs from peridotite xenoliths coming from subduction related geodynamic situations. Accordingly, various melt and fluid migration events could have affected the hydration state and enhanced annealing of the SCLM throughout the last 20 Ma under the Styrian Basin (Figure 7).

Despite variable annealing, the Styrian Basin xenoliths preserve evidence for deformation under lithospheric conditions, and a considerable number of xenoliths show CPO, suggesting deformation under a transpressional regime (Figure 5). In the Eastern Alps, transpressional deformation at crustal levels has been initiated after the break off of the European Plate ~29 Ma ago (Blanckenburg & Davies, 1995; Schmid et al., 2013). Belt-parallel fast *S* wave polarization is observed in most of the Eastern Alps and also at the ARSA station that sample the mantle beneath the Styrian Basin (Qorbani et al., 2015). Belt-parallel *S* wave polarization is often observed in many convergent plate boundaries submitted to transpressional deformation (Vauchez et al., 2012, and references therein). On the other hand, similar NW-SE oriented seismic polarization is observed in the central part of the CPR, ~150 km from the study area (Kovács, Falus, et al., 2012; Qorbani et al., 2016) and these fast polarizations were interpreted as due to asthenospheric flow in response to the northeastward movement of the Adria microplate (Qorbani et al., 2016). However, as the seismic anisotropy integrates the lithosphere and the asthenosphere contributions, these two interpretations might not be contradictory.

To conclude the evolution of the subcontinental lithospheric mantle beneath the Styrian Basin can be outlined in the following steps (summarized in Figure 7): (a) lithosphere thinning prior the Alpine orogeny; decompression affected the garnet-facies lithospheric mantle, which led to the formation of spinel-pyroxene clusters; (b) active subduction of the Penninic slab beneath the Adria/ALCAPA plate until ~35 Ma; (c) the SCLM deformed under transpressional tectonic regime, most probably during the transpressional phase after the Penninic slab breakoff in the Eastern Alps, ~29 Ma ago; due to this deformation event, the foliation and [010]-fiber CPO symmetry of olivines were developed; and (d) during the extension of the Pannonian Basin the previously metasomatized SCLM melted and produced subduction-related volcanism; the release of subduction-related fluids, the migrating intermediate melts impregnated the SCLM, causing extensive annealing. Finally, later alkaline basaltic melts sampled the annealed lithospheric mantle beneath the Styrian Basin.

6. Conclusions

We presented new microstructural, structural hydroxyl content and seismic anisotropy data of spinel facies mantle xenoliths from the westernmost Styrian Basin and discussed the implications of these results to the thermomechanical and geodynamical evolution of the SCLM beneath the western part of the Pannonian Basin. The studied xenoliths display dominantly coarse-grained microstructures with low densities of intracrystalline deformation features but clear olivine and pyroxenes CPO. They represent the sampling of a SCLM that has been deformed and subsequently annealed. The predominance of [010]-fiber olivine CPO, together with the dispersion of the [001] axes of the pyroxenes in the foliation plane, suggests that the deformation occurred in a transpressional regime. One xenolith (the fine-grained equigranular lherzolite GS0611) has a particular microstructure, which we interpreted as recording synkinematic clinopyroxene crystallization in response to localized deformation in the presence of melts.

The structural hydroxyl content of the studied xenoliths exhibits rather high equilibrium values, up to ~10, ~290, and ~675 ppm in olivine, orthopyroxene, and clinopyroxene, respectively. The more annealed olivines contain higher structural hydroxyl than the more deformed ones. Based on the microstructural observations,

thermobarometric and FTIR data, we propose that annealing was enhanced by fluid/melt percolation in the lithospheric mantle.

Based on the average seismic properties of the Styrian Basin mantle peridotites and supposing a transpressional deformation leading to the formation of a vertical foliation and a horizontal lineation, the 50 km thick SCLM in this region may produce up to 0.5 s of shear wave splitting. This is less than half of the measured values in nearby station ARSA, implying that asthenospheric deformation strongly contributes to the measured signal. The belt-parallel fast anisotropy orientations are nevertheless consistent with transpressional deformation of the lithospheric mantle near the suture zone of the Eastern Alps.

The most recent geodynamic event in the region was the Miocene extension leading to the formation of the Pannonian Basin and the subsequent tectonic inversion of the later. However, signs of these recent deformations were not clearly observed in the Styrian Basin xenoliths. In the SB xenoliths the last recorded event is the annealing, which we interpret as associated with the percolation of hydrous melts or fluids. The extensional deformation and subsequent compression were poorly developed in the Styrian Basin that would be consistent with a smaller extension of the lithosphere compared to the central part of the CPR. The fluids favoring the annealing might be related to the subduction episodes, which affected the SCLM, presumably during the Penninic subduction.

Acknowledgments

We acknowledge the constructive criticism and helpful comments of Q-K. Xia, an anonymous reviewer, and the Editor, John Geissman. We are grateful to F. Barou for his assistance during EBSD-SEM analyses. L. E. Aradi is grateful to Bernardo Cesare, Levente Patkó, and Raúl Carampin for their help during the EPMA measurements. The FTIR analyses were carried out with the help of Judith Mihály and Csaba Németh. This research was partially granted by the Hungarian Science Foundation (OTKA, 78425 to Cs. Szabó). K. H.'s work was funded by the European Union Seventh Framework Programme Marie Curie postdoctoral fellowship (grant PIEFGA-2012-327226) and by the Juan de la Cierva Postdoctoral Fellowship (grant FPDI-2013-16253) of the Spanish Ministry of Economic and Competitiveness (MINECO). This project has been implemented with the support provided to I. J. Kovács from the National Research, Development and Innovation Fund of Hungary, financed under the K119740 funding scheme. The data used in this paper are listed in the references, tables, and supporting information. The raw EBSD and geochemical data are available from the corresponding author upon request. The FTIR spectra are available at the PULI (Pannonian Uniform Lithospheric Infrared spectral database) website (http://puli.mfgi.hu/). This is the 86 publication of the Lithosphere Fluid Research Lab (LRG).

References

Abramson, E. H., Brown, J. M., Slutsky, L. J., & Zaug, J. (1997). The elastic constants of San Carlos olivine to 17 GPa. *Journal of Geophysical Research*, *102*(B6), 12,253–12,263. https://doi.org/10.1029/97JB00682

Ali, S., Ntaflos, T., & Upton, B. G. J. (2013). Petrogenesis and mantle source characteristics of Quaternary alkaline mafic lavas in the western Carpathian–Pannonian region, Styria, Austria. *Chemical Geology*, *337–338*, 99–113. https://doi.org/10.1016/j.chemgeo.2012.12.001

Artemieva, I. M. (2009). The continental lithosphere: Reconciling thermal, seismic, and petrologic data. *Lithos*, *109*, 23–46. https://doi.org/10.1016/j.lithos.2008.09.015

Bachmann, F., Hielscher, R., & Schaeben, H. (2010). Texture analysis with MTEX–free and open source software toolbox. *Solid State Phenomena*, *160*, 63–68. https://doi.org/10.4028/www.scientific.net/SSP.160.63

Bada, G., & Horváth, F. (2001). On the structure and tectonic of the Pannonian Basin and surrounding orogens. *Acta Geologica Hungarica*, *44*(2–3), 301–327.

Balan, E., Ingrin, J., Delattre, S., Kovács, I., & Blanchard, M. (2011). Theoretical infrared spectrum of OH-defects in forsterite. *European Journal of Mineralogy*, *23*, 285–292. https://doi.org/10.1127/0935-1221/2011/0023-2090

Bali, E., Szabo, C., Vaselli, O., & Torok, K. (2002). Significance of silicate melt pockets in upper mantle xenoliths from the Bakony-Balaton Highland Volcanic Field, Western Hungary. *Lithos*, *61*(1–2), 79–102. https://doi.org/10.1016/S0024-4937(01)00075-5

Bali, E., Zajacz, Z., Kovács, I., Szabó, C., Halter, W., Vaselli, O., … Bodnar, R. J. (2008). A quartz-bearing orthopyroxene-rich websterite xenolith from the Pannonian Basin, Western Hungary: Evidence for release of quartz-saturated melts from a subducted slab. *Journal of Petrology*, *49*, 421–439. https://doi.org/10.1093/petrology/egm086

Balogh, K., Ebner, F., Ravasz, C., Herrmann, P., Lobitzer, H., & Solti, G. (1994). K/Ar-Alter tertiärer Vulkanite der südöstlichen Steiermark und des südlichen Burgenlandes. *Jubiläumsschrift*, *20*, 55–72.

Baptiste, V., & Tommasi, A. (2014). Petrophysical constraints on the seismic properties of the Kaapvaal craton mantle root. *Solid Earth Discussions*, *5*(2), 963–1005.

Baptiste, V., Tommasi, A., & Demouchy, S. (2012). Deformation and hydration of the lithospheric mantle beneath the Kaapvaal craton, South Africa. *Lithos*, *149*, 31–50. https://doi.org/10.1016/j.lithos.2012.05.001

Baptiste, V., Tommasi, A., Vauchez, A., Demouchy, S., & Rudnick, R. L. (2015). Deformation, hydration, and anisotropy of the lithospheric mantle in an active rift: Constraints from mantle xenoliths from the North Tanzanian divergence of the East African Rift. *Tectonophysics*, *639*, 34–55. https://doi.org/10.1016/j.tecto.2014.11.011

Barruol, G., & Mainprice, D. (1993). A quantitative evaluation of the contribution of crustal rocks to the shear-wave splitting of teleseismic SKS waves. *Physics of the Earth and Planetary Interiors*, *78*(3–4), 281–300. https://doi.org/10.1016/0031-9201(93)90161-2

Barruol, G., Bonnin, M., Pedersen, H., Bokelmann, G. H. R., & Tiberi, C. (2011). Belt-parallel mantle flow beneath a halted continental collision: The Western Alps. *Earth and Planetary Science Letters*, *302*, 429–438. https://doi.org/10.1016/j.epsl.2010.12.040

Bascou, J., Delpech, G., Vauchez, A., Moine, B. N., Cottin, J. Y., & Barruol, G. (2008). An integrated study of microstructural, geochemical, and seismic properties of the lithospheric mantle above the Kerguelen plume (Indian Ocean). *Geochemistry, Geophysics, Geosystems*, *9*, Q04036. https://doi.org/10.1029/2007GC001879

Bell, D. R., & Rossman, G. R. (1992). Water in Earth's mantle: The role of nominally anhydrous minerals. *Science*, *255*(5050), 1391–1397. https://doi.org/10.1126/science.255.5050.1391

Bell, D. R., Ihinger, P. D., & Rossman, G. R. (1995). Quantitative-analysis of trace OH in garnet and pyroxenes. *American Mineralogist*, *80*(5–6), 465–474. https://doi.org/10.2138/am-1995-5-607

Bell, D. R., Rossman, G. R., Maldener, J., Endisch, D., & Rauch, F. (2003). Hydroxide in olivine: A quantitative determination of the absolute amount and calibration of the IR spectrum. *Journal of Geophysical Research*, *108*(B2), 2105. https://doi.org/10.1029/2001JB000679

Ben Ismail, W., & Mainprice, D. (1998). An olivine fabric database: An overview of upper mantle fabrics and seismic anisotropy. *Tectonophysics*, *296*(1–2), 145–157. https://doi.org/10.1016/S0040-1951(98)00141-3

Ben-Ismail, W., Barruol, G., & Mainprice, D. (2001). The Kaapvaal craton seismic anisotropy: Petrophysical analyses of upper mantle kimberlite nodules. *Geophysical Research Letters*, *28*(13), 2497–2500. https://doi.org/10.1029/2000GL012419

Berkesi, M., Guzmics, T., Szabo, C., Dubessy, J., Bodnar, R. J., Hidas, K., & Ratter, K. (2012). The role of CO_2-rich fluids in trace element transport and metasomatism in the lithospheric mantle beneath the central Pannonian Basin, Hungary, based on fluid inclusions in mantle xenoliths. *Earth and Planetary Science Letters*, *331*, 8–20.

Berry, A. J., Hermann, J., O'Neill, H. S., & Foran, G. J. (2005). Fingerprinting the water site in mantle olivine. *Geology*, *33*, 869–872. https://doi.org/10.1130/G21759.1

Bianchi, I., Miller, M. S., & Bokelmann, G. (2014). Insights on the upper mantle beneath the Eastern Alps. *Earth and Planetary Science Letters*, *403*, 199–209. https://doi.org/10.1016/j.epsl.2014.06.051

Blanckenburg, F., & Davies, J. H. (1995). Slab breakoff: A model for syncollisional magmatism and tectonics in the Alps. *Tectonics*, *14*(1), 120–131. https://doi.org/10.1029/94TC02051

Bojar, H.-P., Bojar, A.-V., HałAs, S., & Wójtowicz, A. (2013). K/Ar geochronology of igneous amphibole phenocrysts in Miocene to Pliocene volcaniclastics, Styrian Basin, Austria. *Geological Quarterly*, *57*(3), 405–416.

Bonadiman, C., Hao, Y., Coltorti, M., Dallai, L., Faccini, B., Huang, Y. U., & Xia, Q. (2009). Water contents of pyroxenes in intraplate lithospheric mantle. *European Journal of Mineralogy*, *21*(3), 637–647. https://doi.org/10.1127/0935-1221/2009/0021-1935

Brey, G. P., & Köhler, T. (1990). Geothermobarometry in four-phase Lherzolites II. New thermobarometers, and practical assessment of existing thermobarometers. *Journal of Petrology*, *31*(6), 1353–1378. https://doi.org/10.1093/petrology/31.6.1353

Brückl, E. (2011). Lithospheric structure and tectonics of the Eastern Alps—Evidence from new seismic data. In *Tectonics*. (Chapter 2, pp. 39–64). InTech. https://doi.org/10.5772/14364

Bunge, H. J. (1982). *Texture analysis in materials sciences* (p. 59). London, UK: Butterworth's.

Carter, N. L., & Avé Lallemant, H. G. (1970). High temperature flow of dunite and peridotite. *Bulletin of the Geological Society of America*, *81*(8), 2181–2202. https://doi.org/10.1130/0016-7606(1970)81%5B2181:HTFODA%5D2.0.CO;2

Chalot-Prat, F., & Boullier, A.-M. (1997). Metasomatism in the subcontinental mantle beneath the eastern Carpathians (Romania): New evidence from trace element geochemistry. *Contributions to Mineralogy and Petrology*, *129*(4), 284–307. https://doi.org/10.1007/s004100050338

Coltorti, M., Bonadiman, C., Faccini, B., Ntaflos, T., & Siena, F. (2007). Slab melt and intraplate metasomatism in Kapfenstein mantle xenoliths (Styrian Basin, Austria). *Lithos*, *94*, 66–89. https://doi.org/10.1016/j.lithos.2006.07.003

Couvy, H., Frost, D. J., Heidelbach, F., Nyilas, K., Ungár, T., Mackwell, S., & Cordier, P. (2004). Shear deformation experiments of forsterite at 11 GPa–1400°C in the multianvil apparatus. *European Journal of Mineralogy*, *16*, 877–889. https://doi.org/10.1127/0935-1221/2004/0016-0877

Créon, L., et al. (2017). Highly CO_2-supersaturated melts in the Pannonian lithospheric mantle—A transient carbon reservoir? *Lithos*, *286*(Supplement C), 519–533.

Csontos, L., & Vörös, A. (2004). Mesozoic plate tectonic reconstruction of the Carpathian region. *Palaeogeography Palaeoclimatology Palaeoecology*, *210*, 1–56. https://doi.org/10.1016/j.palaeo.2004.02.033

Dando, B. D. E., Stuart, G. W., Houseman, G. A., Hegedüs, E., Brückl, E., & Radovanović, S. (2011). Teleseismic tomography of the mantle in the Carpathian–Pannonian region of central Europe. *Geophysical Journal International*, *186*, 11–31. https://doi.org/10.1111/j.1365-246X.2011.04998.x

Dégi, J., Abart, R., Török, K., Bali, E., Wirth, R., & Rhede, D. (2009). Symplectite formation during decompression induced garnet breakdown in lower crustal mafic granulite xenoliths: Mechanisms and rates. *Contributions to Mineralogy and Petrology*, *159*, 293–314.

Della Ventura, G., Oberti, R., Hawthorne, F. C., & Bellatreccia, F. (2007). FTIR spectroscopy of Ti-rich pargasites from Lherz and the detection of O_2 at the anionic O3 site in amphiboles. *American Mineralogist*, *92*, 1645–1651. https://doi.org/10.2138/am.2007.2199

Demouchy, S., & Bolfan-Casanova, N. (2016). Distribution and transport of hydrogen in the lithospheric mantle: A review. *Lithos*, *240–243*, 402–425. https://doi.org/10.1016/j.lithos.2015.11.012

Demouchy, S., Tommasi, A., Boffa Ballaran, T., & Cordier, P. (2013). Low strength of Earth's uppermost mantle inferred from tri-axial deformation experiments on dry olivine crystals. *Physics of the Earth and Planetary Interiors*, *220*(0), 37–49. https://doi.org/10.1016/j.pepi.2013.04.008

Demouchy, S., Mussi, A., Barou, F., Tommasi, A., & Cordier, P. (2014). Viscoplasticity of polycrystalline olivine experimentally deformed at high pressure and 900°C. *Tectonophysics*, *623*, 123–135. https://doi.org/10.1016/j.tecto.2014.03.022

Demouchy, S., Ishikawa, A., Tommasi, A., Alard, O., & Keshav, S. (2015). Characterization of hydration in the mantle lithosphere: Peridotite xenoliths from the Ontong Java Plateau as an example. *Lithos*, *212–215*, 189–201. https://doi.org/10.1016/j.lithos.2014.11.005

Denis, C. M. M., Alard, O., & Demouchy, S. (2015). Water content and hydrogen behaviour during metasomatism in the uppermost mantle beneath Ray Pic volcano (Massif Central, France). *Lithos*, *236–237*, 256–274. https://doi.org/10.1016/j.lithos.2015.08.013

Denis, C. M. M., Demouchy, S., & Shaw, C. S. J. (2013). Evidence of dehydration in peridotites from Eifel Volcanic Field and estimates of the rate of magma ascent. *Journal of Volcanology and Geothermal Research*, *258*, 85–99.

Dobosi, G., Schultz-Güttler, R., Kurat, G., & Kracher, A. (1991). Pyroxene chemistry and evolution of alkali basaltic rocks from Burgenland and Styria, Austria. *Mineralogy and Petrology*, *43*(4), 275–292. https://doi.org/10.1007/BF01164531

Dobosi, G., Jenner, G., Embey-Isztin, A., & Downes, H. (2010). Cryptic metasomatism in clino- and orthopyroxene in the upper mantle beneath the Pannonian region. In M.–Coltorti (Eds.), *Petrological evolution of the European lithospheric mantle: From Archaean to present day*. *Geological Society, London, Special Publications* (Vol. 337, pp. 177–194). https://doi.org/10.1144/SP337.9

Dobosi, G., Kurat, G., Jenner, G. A., & Brandstätter, F. (1999). Cryptic metasomatism in the upper mantle beneath Southeastern Austria: A laser ablation microprobe-ICP-MS study. *Mineralogy and Petrology*, *67*(3), 143–161.

Dombrádi, E., Sokoutis, D., Bada, G., Cloetingh, S., & Horváth, F. (2010). Modelling recent deformation of the Pannonian lithosphere: Lithospheric folding and tectonic topography. *Tectonophysics*, *484*, 103–118. https://doi.org/10.1016/j.tecto.2009.09.014

Downes, H., Embey-Isztin, A., & Thirlwall, M. F. (1992). Petrology and geochemistry of spinel peridotite xenoliths from the western Pannonian Basin (Hungary): Evidence for an association between enrichment and texture in the upper mantle. *Contributions to Mineralogy and Petrology*, *109*(3), 340–354. https://doi.org/10.1007/BF00283323

Ebner, F., & Sachsenhofer, R. F. (1995). Palaeogeography, subsidence and thermal history of the Neogene Styrian Basin (Pannonian basin system, Austria). *Tectonophysics*, *242*(1–2), 133–150. https://doi.org/10.1016/0040-1951(94)00155-3

Embey-Isztin, A. (1976). Amphibole/lherzolite composite xenoliths from Szigliget, north of Lake Balaton, Hungary. *Earth and Planetary Science Letters*, *31*(2), 297–304. https://doi.org/10.1016/0012-821X(76)90223-5

Embey-Isztin, A. (1978). On the petrology of spinel lherzolite nodules in basaltic rocks from Hungary and Auvergne, France. *Annalen des Naturhistorischen Museums Hungarica*, *70*, 27–44.

Embey-Isztin, A. (1984). Texture types and their relative frequencies in ultramafic and mafic xenoliths from Hungarian alkali basaltic rocks. *Annales Historico-Naturales Musei Nationalis Hungarici*, *76*, 27–42.

Embey-Isztin, A., & Dobosi, G. (1995). Mantle source characteristics for Miocene-Pleistocene alkali basalts, Carpathian-Pannonian region: A review of trace elements and isotopic composition. In H. Downes & O. Vaselli (Eds.), *Neogene and related volcanism in the Carpatho-Pannonian region*, (pp. 155–166). Roma, Pisa: Acta Vulcanologica.

Embey-Isztin, A., Scharbert, H. G., Dietrich, H., & Poultidis, H. (1989). Petrology and geochemistry of peridotite xenoliths in alkali basalts from the Transdanubian Volcanic Region, West Hungary. *Journal of Petrology*, *30*(1), 79–105. https://doi.org/10.1093/petrology/30.1.79

Embey-Isztin, A., Downes, H., James, D. E., Upton, B. G. J., Dobosi, G., Ingram, G. A., … Scharbert, H. G. (1993). The petrogenesis of Pliocene alkaline volcanic rocks from the Pannonian Basin, eastern Central Europe. *Journal of Petrology*, *34*(2), 317–343. https://doi.org/10.1093/petrology/34.2.317

Embey-Isztin, A., Dobosi, G., Altherr, R., & Meyer, H. P. (2001). Thermal evolution of the lithosphere beneath the western Pannonian Basin: Evidence from deep-seated xenoliths. *Tectonophysics*, *331*(3), 285–306. https://doi.org/10.1016/S0040-1951(00)00287-0

Embey-Isztin, A., Dobosi, G., Bodinier, J.-L., Bosch, D., Jenner, G. A., Pourtales, S., & Bruguier, O. (2014). Origin and significance of poikilitic and mosaic peridotite xenoliths in the western Pannonian Basin: Geochemical and petrological evidences. *Contributions to Mineralogy and Petrology*, *168*(3), 1054. https://doi.org/10.1007/s00410-014-1054-y

Falus, G., Szabó, C., & Vaselli, O. (2000). Mantle upwelling within the Pannonian Basin: Evidence from xenolith lithology and mineral chemistry. *Terra Nova*, *12*(6), 295–302. https://doi.org/10.1046/j.1365-3121.2000.00313.x

Falus, G., Szabo, C., Kovacs, I., Zajacz, Z., & Halter, W. (2007). Symplectite in spinel lherzolite xenoliths from the Little Hungarian Plain, Western Hungary: A key for understanding the complex history of the upper mantle of the Pannonian Basin. *Lithos*, *94*, 230–247. https://doi.org/10.1016/j.lithos.2006.06.017

Falus, G., Tommasi, A., Ingrin, J., & Szabó, C. (2008). Deformation and seismic anisotropy of the lithospheric mantle in the southeastern Carpathians inferred from the study of mantle xenoliths. *Earth and Planetary Science Letters*, *272*, 50–64. https://doi.org/10.1016/j.epsl.2008.04.035

Falus, G., Tommasi, A., & Soustelle, V. (2011). The effect of dynamic recrystallization on olivine crystal preferred orientations in mantle xenoliths deformed under varied stress conditions. *Journal of Structural Geology*, *33*, 1528–1540. https://doi.org/10.1016/j.jsg.2011.09.010

Faul, U. H., Cline, C. J., David, E. C., Berry, A. J., & Jackson, I. (2016). Titanium-hydroxyl defect-controlled rheology of the Earth's upper mantle. *Earth and Planetary Science Letters*, *452*, 227–237. https://doi.org/10.1016/j.epsl.2016.07.016

Fodor, L., Csontos, L., Bada, G., Györfi, I., & Benkovics, L. (1999). Tertiary tectonic evolution of the Pannonian basin system and neighbouring orogens: A new synthesis of palaeostress data. In B. Durand et al., *The Mediterranean basins: Tertiary extension within the Alpine orogen*. *Geological Society, London, Special Publications* (Vol. 156, pp. 295–334).

Gavrilenko, P. (2008). Water solubility in diopside, PhD thesis, Bayerisches Geoinst., Univ. Bayreuth, Bayreuth, Germany.

Grad, M., & Tiira, T. (2009). The Moho depth map of the European Plate. *Geophysical Journal International*, *176*, 279–292. https://doi.org/10.1111/j.1365-246X.2008.03919.x

Grant, K., Ingrin, J., Lorand, J. P., & Dumas, P. (2007). Water partitioning between mantle minerals from peridotite xenoliths. *Contributions to Mineralogy and Petrology*, *154*, 15–34. https://doi.org/10.1007/s00410-006-0177-1

Green, D. H., Hibberson, W. O., Kovács, I., & Rosenthal, A. (2010). Water and its influence on the lithosphere-asthenosphere boundary. *Nature*, *467*, 448–451. https://doi.org/10.1038/nature09369

Hansen, L. N., Zhao, Y.-H., Zimmerman, M. E., & Kohlstedt, D. L. (2014). Protracted fabric evolution in olivine: Implications for the relationship among strain, crystallographic fabric, and seismic anisotropy. *Earth and Planetary Science Letters*, *387*, 157–168. https://doi.org/10.1016/j.epsl.2013.11.009

Hao, Y., Xia, Q., Li, Q., Chen, H., & Feng, M. (2014). Partial melting control of water contents in the Cenozoic lithospheric mantle of the Cathaysia block of South China. *Chemical Geology*, *380*, 7–19. https://doi.org/10.1016/j.chemgeo.2014.04.017

Hao, Y.-T., Xia, Q.-K., Tian, Z.-Z., & Liu, J. (2016). Mantle metasomatism did not modify the initial H_2O content in peridotite xenoliths from the Tianchang basalts of eastern China. *Lithos*, *260*, 315–327. https://doi.org/10.1016/j.lithos.2016.06.003

Harangi, S. (2001). Neogene magmatism in the Alpine-Pannonian transition zone—A model for melt generation in a complex geodynamic setting. *Acta Vulcanologica*, *13*(1), 25–39.

Harangi, S., & Lenkey, L. (2007). Genesis of the Neogene to quaternary volcanism in the Carpathian-Pannonian region: Role of subduction, extension, and mantle plume. In L. Beccaluva, G. Bianchini, & M. Wilson (Eds.), *Special paper 418: Cenozoic volcanism in the Mediterranean area* (pp. 67–92). Boulder, CO: https://doi.org/10.1130/2007.2418(04)

Harangi, S., Wilson, M., & Tonarini, S. (1995). Petrogenesis of Neogene potassic volcanic rocks in the Pannonian Basin. *Acta Vulcanologica*, *7*(2), 125–134.

Harangi, S., Jankovics, M. É., Sági, T., Kiss, B., Lukács, R., & Soós, I. (2015). Origin and geodynamic relationships of the late Miocene to Quaternary alkaline basalt volcanism in the Pannonian Basin, eastern–central Europe. *International Journal of Earth Sciences*, *104*(8), 2007–2032. https://doi.org/10.1007/s00531-014-1105-7

Heritsch, H. (1967). Über die Magmenentfaltung des steirisches Vulkanbogens. *Contributions to Mineralogy and Petrology*, *15*(4), 330–344. https://doi.org/10.1007/BF00404200

Hidas, K., Falus, G., Szabó, C., Szabó, P. J., Kovács, I., & Földes, T. (2007). Geodynamic implications of flattened tabular equigranular textured peridotites from the Bakony-Balaton Highland Volcanic Field (Western Hungary). *Journal of Geodynamics*, *43*, 484–503. https://doi.org/10.1016/j.jog.2006.10.007

Hidas, K., Guzmics, T., Szabo, C., Kovacs, I., Bodnar, R. J., Zajacz, Z., … Perucchi, A. (2010). Coexisting silicate melt inclusions and H_2O-bearing, CO_2-rich fluid inclusions in mantle peridotite xenoliths from the Carpathian-Pannonian region (central Hungary). *Chemical Geology*, *274*, 1–18. https://doi.org/10.1016/j.chemgeo.2010.03.004

Hidas, K., Konc, Z., Garrido, C. J., Tommasi, A., Vauchez, A., Padrón-Navarta, J. A., … Gervilla, F. (2016). Flow in the western Mediterranean shallow mantle: Insights from xenoliths in Pliocene alkali basalts from SE Iberia (eastern Betics, Spain). *Tectonics*, *35*, 2657–2676. https://doi.org/10.1002/2016TC004165

Hidas, K., Tommasi, A., Garrido, C. J., Padrón-Navarta, J. A., Mainprice, D., Vauchez, A., … Marchesi, C. (2016). Fluid-assisted strain localization in the shallow subcontinental lithospheric mantle. *Lithos*, *262*, 636–650. https://doi.org/10.1016/j.lithos.2016.07.038

Hielscher, R., & Schaeben, H. (2008). A novel pole figure inversion method: Specification of the MTEX algorithm. *Journal of Applied Crystallography*, *41*, 1024–1037. https://doi.org/10.1107/S0021889808030112

Higgie, K., & Tommasi, A. (2012). Feedbacks between deformation and melt distribution in the crust–mantle transition zone of the Oman ophiolite. *Earth and Planetary Science Letters*, *359–360*, 61–72. https://doi.org/10.1016/j.epsl.2012.10.003

Higgie, K., & Tommasi, A. (2014). Deformation in a partially molten mantle: Constraints from plagioclase lherzolites from Lanzo, Western Alps. *Tectonophysics*, *615–616*, 167–181. https://doi.org/10.1016/j.tecto.2014.01.007

Horváth, F., Bada, G., Szafián, P., Tari, G., & Ádám, A. (2006). Formation and deformation of the Pannonian Basin: Constraints from observational data. In D. G. Gee & R. Stephenson (Eds.), *European lithosphere dynamics* (pp. 191–206). London: The Geological Society of London.

Horváth, F., Musitz, B., Balázs, A., Végh, A., Uhrin, A., Nádor, A., … Wórum, G. (2015). Evolution of the Pannonian basin and its geothermal resources. *Geothermics*, *53*, 328–352. https://doi.org/10.1016/j.geothermics.2014.07.009

Huismans, R. S., Podladchikov, Y. Y., & Cloetingh, S. (2001). Dynamic modeling of the transition from passive to active rifting, application to the Pannonian basin. *Tectonics*, *20*(6), 1021–1039. https://doi.org/10.1029/2001TC900010

Isaak, D. G., Ohno, I., & Lee, P. C. (2006). The elastic constants of monoclinic single-crystal chrome-diopside to 1,300 K. *Physics and Chemistry of Minerals*, *32*, 691–699. https://doi.org/10.1007/s00269-005-0047-9

Jackson, J. M., Sinogeikin, S. V., & Bass, J. D. (2007). Sound velocities and single-crystal elasticity of orthoenstatite to 1073°K at ambient pressure. *Physics of the Earth and Planetary Interiors*, *161*, 1–12. https://doi.org/10.1016/j.pepi.2006.11.002

Jugovics, L. (1915). Az Alpok keleti végződése alján és a Vas vármegyei Kis Magyar Alföldön felbukkanó bazaltok és bazalttufák, I. rész, Magyar Állami Földtani Intézet Éves Jelentése(1915), 49–73.

Jugovics, L. (1916). Az Alpok keleti végződése alján és a veszprémmegyei Kis Magyar Alföldön felbukkanó bazaltok és bazalttufák, II. rész, Magyar Állami Földtani Intézet Éves Jelentése(1916), 63–76.

Jung, H., & Karato, S.-I. (2001). Water-induced fabric transitions in olivine. *Science*, *293*(5534), 1460–1463. https://doi.org/10.1126/science.1062235

Kaczmarek, M.-A., & Tommasi, A. (2011). Anatomy of an extensional shear zone in the mantle, Lanzo massif, Italy. *Geochemistry, Geophysics, Geosystems*, *12*, Q0AG06. https://doi.org/10.1029/2011GC003627

Karato, S.-I., Jung, H., Katayama, I., & Skemer, P. (2008). Geodynamic significance of seismic anisotropy of the upper mantle: New insights from laboratory studies. *Annual Review of Earth and Planetary Sciences*, *36*, 59–95. https://doi.org/10.1146/annurev.earth.36.031207.124120

Kázmér, M., & Kovács, S. (1985). Permian-Palaeogene paleogeography along the eastern part of the Insubric-Periariatic lineament system: Evidence for continental escape of the Bakony-Drauzug unit. *Acta Geologica Hungarica*, *28*, 71–84.

Klébesz, R., Gráczer, Z., Szanyi, G., Liptai, N., Kovács, I., Patkó, L., … Szabó, C. (2015). Constraints on the thickness and seismic properties of the lithosphere in an extensional setting (Nógrád-Gömör volcanic field, northern Pannonian Basin). *Acta Geodaetica et Geophysica*, *50*(2), 133–149. https://doi.org/10.1007/s40328-014-0094-0

Konecný, V., Lexa, J., Balogh, K., & Konecný, P. (1995). Alkali basalt volcanism in southern Slovakia: Volcanic forms and time evolution. In H. Downes & O. Vaselli (Eds.), *Neogene and related magmatism in the Carpatho-Pannonian region* (Vol. 7, pp. 167–171). Acta Volcanologica. Roma, Pisa.

Kourim, F., Vauchez, A., Bodinier, J.-L., Alard, O., & Bendaoud, A. (2015). Subcontinental lithosphere reactivation beneath the Hoggar swell (Algeria): Localized deformation, melt channeling and heat advection. *Tectonophysics*, *650*, 18–33. https://doi.org/10.1016/j.tecto.2014.11.012

Kovács, I., & Szabó, C. (2008). Middle Miocene volcanism in the vicinity of the middle Hungarian zone: Evidence for an inherited enriched mantle source. *Journal of Geodynamics*, *45*, 1–17. https://doi.org/10.1016/j.jog.2007.06.002

Kovács, I., Hermann, J., O'Neill, H. S. C., Gerald, J. F., Sambridge, M., & Horváth, G. (2008). Quantitative absorbance spectroscopy with unpolarized light: Part II. Experimental evaluation and development of a protocol for quantitative analysis of mineral IR spectra. *American Mineralogist*, *93*, 765–778. https://doi.org/10.2138/am.2008.2656

Kovács, I., O'Neill, H. S. C., Hermann, J., & Hauri, E. H. (2010). Site-specific infrared O-H absorption coefficients for water substitution into olivine. *American Mineralogist*, *95*, 292–299. https://doi.org/10.2138/am.2010.3313

Kovács, I., Falus, G., Stuart, G., Hidas, K., Szabó, C., Flower, M. J., … Zilahi-Sebess, L. (2012). Seismic anisotropy and deformation patterns in upper mantle xenoliths from the central Carpathian–Pannonian region: Asthenospheric flow as a driving force for Cenozoic extension and extrusion? *Tectonophysics*, *514–517*, 168–179. https://doi.org/10.1016/j.tecto.2011.10.022

Kovács, I., Green, D. H., Rosenthal, A., Hermann, J., O'Neill, H. S. C., Hibberson, W. O., & Udvardi, B. (2012). An experimental study of water in nominally anhydrous minerals in the upper mantle near the water-saturated solidus. *Journal of Petrology*, *53*, 2067–2093. https://doi.org/10.1093/petrology/egs044

Kovács, I., Lenkey, L., Green, D. H., Fancsik, T., Falus, G., Kiss, J., … Vikor, Z. (2017). The role of pargasitic amphibole in the formation of major geophysical discontinuities in the shallow upper mantle. *Acta Geodaetica et Geophysica*, *52*(2), 183–204. https://doi.org/10.1007/s40328-016-0191-3

Kröll, A. (1988). Prätertiärer Untergrund des Steirischen Beckens und der Südburgenländischen Schwelle 1: 200.000, Geologische Themenkarte, Verlag der Geologischen Bundesanstalt, Vienna, Austria.

Kruckenberg, S. C., Tikoff, B., Toy, V. G., Newman, J., & Young, L. I. (2013). Strain localization associated with channelized melt migration in upper mantle lithosphere: Insights from the Twin Sisters ultramafic complex, Washington, USA. *Journal of Structural Geology*, *50*, 133–147. https://doi.org/10.1016/j.jsg.2012.10.009

Kurat, G., Palme, H., Spettel, B., Baddenhausen, H., Hofmeister, H., Palme, C., & Wanke, H. (1980). Geochemistry of ultramafic xenoliths from Kapfenstein, Austria—Evidence for a variety of upper mantle processes. *Geochimica et Cosmochimica Acta*, *44*(1), 45–60. https://doi.org/10.1016/0016-7037(80)90176-3

Kurat, G., Embeyisztin, A., Kracher, A., & Scharbert, H. G. (1991). The upper mantle beneath Kapfenstein and the Transdanubian Volcanic Region, E Austria and W Hungary—A comparison. *Mineralogy and Petrology*, *44*(1–2), 21–38. https://doi.org/10.1007/BF01167098

Le Roux, V., Bodinier, J. L., Tommasi, A., Alard, O., Dautria, J. M., Vauchez, A., & Riches, A. J. V. (2007). The Lherz spinel lherzolite: Refertilized rather than pristine mantle. *Earth and Planetary Science Letters*, *259*, 599–612. https://doi.org/10.1016/j.epsl.2007.05.026

Le Roux, V., Tommasi, A., & Vauchez, A. (2008). Feedback between melt percolation and deformation in an exhumed lithosphere–asthenosphere boundary. *Earth and Planetary Science Letters*, *274*, 401–413. https://doi.org/10.1016/j.epsl.2008.07.053

Lenkey, L., Dövényi, P., Horváth, F., & Cloetingh, S. (2002). Geothermics of the Pannonian Basin and its bearing on the neotectonics. *EGU Stephan Mueller Special Publications Series*, *3*, 29–40.

Li, Z.-X. A., Lee, C.-T. A., Peslier, A. H., Lenardic, A., & Mackwell, S. J. (2008). Water contents in mantle xenoliths from the Colorado Plateau and vicinity: Implications for the mantle rheology and hydration-induced thinning of continental lithosphere. *Journal of Geophysical Research*, *113*, B09210. https://doi.org/10.1029/2007JB005540

Li, P., Xia, Q.-K., Deloule, E., Chen, H., Gu, X.-Y., & Feng, M. (2015). Temporal variation of H_2O content in the lithospheric mantle beneath the eastern North China Craton: Implications for the destruction of cratons. *Gondwana Research*, *28*(1), 276–287. https://doi.org/10.1016/j.gr.2014.03.012

Lippitsch, R. (2003). Upper mantle structure beneath the Alpine orogen from high-resolution teleseismic tomography. *Journal of Geophysical Research*, *108*(B8), 2376. https://doi.org/10.1029/2002JB002016

Liptai, N., Jung, H., Park, M., & Szabó, C. (2013). Olivinorientáció-vizsgálatok a nógrád-gömöri vulkáni terület déli részéről származó felsőköpeny eredetű xenolitokban, *in Hungarian*. *Földtani Közlöny*, *143*, 371–382.

Liptai, N., Patkó, L., Kovács, I. J., Hidas, K., Pintér, Z., Jeffries, T., … Szabó, C. (2017). Multiple Metasomatism beneath the Nógrád–Gömör Volcanic Field (Northern Pannonian Basin) revealed by upper mantle peridotite xenoliths. *Journal of Petrology*, *58*(6), 1107–1144. https://doi.org/10.1093/petrology/egx048

Mainprice, D. (1990). A FORTRAN program to calculate seismic anisotropy from the lattice preferred orientation of minerals. *Computers & Geosciences*, *16*(3), 385–393. https://doi.org/10.1016/0098-3004(90)90072-2

Mainprice, D., Barruol, G., & Ismail, W. B. (2000). *The seismic anisotropy of the Earth's mantle: from single crystal to polycrystal, Earth's deep interior: Mineral physics and tomography from the atomic to the global scale*. Washington, DC: American Geophysical Union.

Mainprice, D., Tommasi, A., Couvy, H., Cordier, P., & Frost, D. J. (2005). Pressure sensitivity of olivine slip systems and seismic anisotropy of Earth's upper mantle. *Nature*, *433*, 731–733. https://doi.org/10.1038/nature03266

Mainprice, D., Hielscher, R., & Schaeben, H. (2011). Calculating anisotropic physical properties from texture data using the MTEX open-source package. *Geological Society, London, Special Publications*, *360*, 175–192. https://doi.org/10.1144/SP360.10

Mainprice, D., Bachmann, F., Hielscher, R., & Schaeben, H. (2014). Descriptive tools for the analysis of texture projects with large datasets using MTEX: Strength, symmetry and components. *Geological Society, London, Special Publications*, *409*(1), 251–271.

Michibayashi, K., Mainprice, D., Fujii, A., Uehara, S., Shinkai, Y., Kondo, Y., … Ji, S. (2016). Natural olivine crystal-fabrics in the western Pacific convergence region: A new method to identify fabric type. *Earth and Planetary Science Letters*, *443*, 70–80. https://doi.org/10.1016/j.epsl.2016.03.019

Mitterbauer, U., Behm, M., Brückl, E., Lippitsch, R., Guterch, A., Keller, G. R., … Šumanovac, F. (2011). Shape and origin of the East-Alpine slab constrained by the ALPASS teleseismic model. *Tectonophysics*, *510*, 195–206. https://doi.org/10.1016/j.tecto.2011.07.001

Nimis, P., & Grütter, H. (2010). Internally consistent geothermometers for garnet peridotites and pyroxenites. *Contributions to Mineralogy and Petrology*, *159*, 411–427. https://doi.org/10.1007/s00410-009-0455-9

Obata, M., & Ozawa, K. (2011). Topotaxic relationships between spinel and pyroxene in kelyphite after garnet in mantle-derived peridotites and their implications to reaction mechanism and kinetics. *Mineralogy and Petrology*, *101*, 217–224. https://doi.org/10.1007/s00710-011-0145-y

O'Reilly, S., & Griffin, W. (1996). 4-D lithosphere mapping: A review of methodology with examples. *Tectonophysics*, *262*(1–4), 3–18. https://doi.org/10.1016/0040-1951(96)00010-8

Padrón-Navarta, J. A., Hermann, J., & O'Neill, H. S. C. (2014). Site-specific hydrogen diffusion rates in forsterite. *Earth and Planetary Science Letters*, *392*, 100–112. https://doi.org/10.1016/j.epsl.2014.01.055

Pera, E., Mainprice, D., & Burlini, L. (2003). Anisotropic seismic properties of the upper mantle beneath the Torre Alfina area (Northern Apennines, Central Italy). *Tectonophysics*, *370*(1–4), 11–30. https://doi.org/10.1016/S0040-1951(03)00175-6

Pintér, Z., Patkó, L., Tene Djoukam, J. F., Kovács, I., Tchouankoue, J. P., Falus, G., … Jeffries, T. (2015). Characterization of the sub-continental lithospheric mantle beneath the Cameroon volcanic line inferred from alkaline basalt hosted peridotite xenoliths from Barombi Mbo and Nyos Lakes. *Journal of African Earth Sciences*, *111*, 170–193. https://doi.org/10.1016/j.jafrearsci.2015.07.006

Pöschl, I. (1991). A model for the depositional evolution of the volcaniclastic succession of a pliocene maar volcano in the Styrian basin, Austria. *Jahrbuch des Geologischen Bundesanstallt*, *134/4*, 809–843. Wien

Qorbani, E., Bianchi, I., & Bokelmann, G. (2015). Slab detachment under the Eastern Alps seen by seismic anisotropy. *Earth and Planetary Science Letters*, *409*, 96–108. https://doi.org/10.1016/j.epsl.2014.10.049

Qorbani, E., Bokelmann, G., Kovács, I., Horváth, F., & Falus, G. (2016). Deformation in the asthenospheric mantle beneath the Carpathian-Pannonian region. *Journal of Geophysical Research: Solid Earth*, *121*, 6644–6657. https://doi.org/10.1002/2015JB012604

Raterron, P., Wu, Y., Weidner, D. J., & Chen, J. (2004). Low-temperature olivine rheology at high pressure. *Physics of the Earth and Planetary Interiors*, *145*, 149–159. https://doi.org/10.1016/j.pepi.2004.03.007

Ratschbacher, L., Frisch, W., Linzer, H.-G., & Marle, O. (1991). Lateral extrusion in the Eastern Alps, Part 2: Structural analysis. *Tectonics*, *10*(2), 257–271. https://doi.org/10.1029/90TC02623

Ratschbacher, L., Merie, O., Davy, P., & Cobbold, P. (1991). Lateral extrusion in the Eastern Alps, Part1: Boundary conditions and experiments scaled for gravity. *Tectonics*, *10*(2), 245–256. https://doi.org/10.1029/90TC02622

Richter, W. (1971). Ariégite, spinell-peridotite und phlogopit-klinopyroxenite aus dem Tuff von Tobaj im Südlichen Burgenland. *Mineralogy and Petrology*, *16*(4), 227–251.

Sachsenhofer, R. F., Lankreijer, A., Cloetingh, S., & Ebner, F. (1997). Subsidence analysis and quantitative basin modelling in the Styrian Basin (Pannonian Basin System, Austria). *Tectonophysics*, *272*(2–4), 175–196. https://doi.org/10.1016/S0040-1951(96)00257-0

Sambridge, M., Gerald, J. F., Kovacs, I., O'Neill, H. S. C., & Hermann, J. (2008). Quantitative absorbance spectroscopy with unpolarized light: Part I. Physical and mathematical development. *American Mineralogist*, *93*, 751–764. https://doi.org/10.2138/am.2008.2657

Schmadicke, E., Gose, J., Witt-Eickschen, G., & Bratz, H. (2013). Olivine from spinel peridotite xenoliths: Hydroxyl incorporation and mineral composition. *American Mineralogist*, *98*(10), 1870–1880. https://doi.org/10.2138/am.2013.4440

Schmid, S. M., Bernoulli, D., Fügenschuh, B., Matenco, L., Schefer, S., Schuster, R., … Ustaszewski, K. (2008). The Alpine-Carpathian-Dinaridic orogenic system: Correlation and evolution of tectonic units. *Swiss Journal of Geosciences*, *101*, 139–183. https://doi.org/10.1007/s00015-008-1247-3

Schmid, S. M., Scharf, A., Handy, M. R., & Rosenberg, C. L. (2013). The Tauern Window (Eastern Alps, Austria): A new tectonic map, with cross-sections and a tectonometamorphic synthesis. *Swiss Journal of Geosciences*, *106*(1), 1–32. https://doi.org/10.1007/s00015-013-0123-y

Soustelle, V., Tommasi, A., Bodinier, J. L., Garrido, C. J., & Vauchez, A. (2009). Deformation and reactive melt transport in the mantle lithosphere above a large-scale partial melting domain: The Ronda peridotite massif, Southern Spain. *Journal of Petrology*, *50*, 1235–1266. https://doi.org/10.1093/petrology/egp032

Stalder, R., & Ludwig, T. (2007). OH incorporation in synthetic diopside. *European Journal of Mineralogy*, *19*, 373–380. https://doi.org/10.1127/0935-1221/2007/0019-1721

Szabó, C., & Taylor, L. A. (1994). Mantle petrology and geochemistry beneath the Nógrád-Gömör volcanic field, Carpathian-Pannonian region. *International Geology Review*, *36*(4), 328–358. https://doi.org/10.1080/00206819409465465

Szabó, C., Falus, G., Zajacz, Z., Kovács, I., & Bali, E. (2004). Composition and evolution of lithosphere beneath the Carpathian–Pannonian region: A review. *Tectonophysics*, *393*, 119–137. https://doi.org/10.1016/j.tecto.2004.07.031

Tari, G., & Horváth, F. (2010). Eo-Alpine evolution of the Transdanubian range in the nappe system of the Eastern Alps: Revival of a 15 years old tectonic model. *Földtani Közlöny*, *140*, 483–510.

Tollan, P. M. E., Smith, R., O'Neill, H. S. C., & Hermann, J. (2017). The responses of the four main substitution mechanisms of H in olivine to H_2O activity at 1050°C and 3 GPa. *Progress in Earth and Planetary Science*, *4*(1), 14. https://doi.org/10.1186/s40645-017-0128-7

Tommasi, A., & Ishikawa, A. (2014). Microstructures, composition, and seismic properties of the Ontong Java Plateau mantle root. *Geochemistry, Geophysics, Geosystems*, *15*, 4547–4569. https://doi.org/10.1002/2014GC005452

Tommasi, A., & Vauchez, A. (2015). Heterogeneity and anisotropy in the lithospheric mantle. *Tectonophysics*, *661*, 11–37. https://doi.org/10.1016/j.tecto.2015.07.026

Tommasi, A., Vauchez, A., Fernandes, L. A., & Porcher, C. C. (1994). Magma-assisted strain localization in an orogen-parallel. *Tectonics*, *13*(2), 421–437. https://doi.org/10.1029/93TC03319

Tommasi, A., Tikoff, B., & Vauchez, A. (1999). Upper mantle tectonics: Three-dimensional deformation, olivine crystallographic fabrics and seismic properties. *Earth and Planetary Science Letters*, *168*(1–2), 173–186. https://doi.org/10.1016/S0012-821X(99)00046-1

Tommasi, A., Mainprice, D., Canova, G., & Chastel, Y. (2000). Viscoplastic self-consistent and equilibrium-based modeling of olivine lattice preferred orientations: Implications for the upper mantle seismic anisotropy. *Journal of Geophysical Research*, *105*(B4), 7893–7908. https://doi.org/10.1029/1999JB900411

Tommasi, A., Vauchez, A., Godard, M., & Belley, F. (2006). Deformation and melt transport in a highly depleted peridotite massif from the Canadian Cordillera: Implications to seismic anisotropy above subduction zones. *Earth and Planetary Science Letters*, *252*, 245–259. https://doi.org/10.1016/j.epsl.2006.09.042

Tommasi, A., Vauchez, A., & Ionov, D. A. (2008). Deformation, static recrystallization, and reactive melt transport in shallow subcontinental mantle xenoliths (Tok Cenozoic volcanic field, SE Siberia). *Earth and Planetary Science Letters*, *272*, 65–77. https://doi.org/10.1016/j.epsl.2008.04.020

Tommasi, A., Baptiste, V., Vauchez, A., & Holtzman, B. (2016). Deformation, annealing, reactive melt percolation, and seismic anisotropy in the lithospheric mantle beneath the southeastern Ethiopian rift: Constraints from mantle xenoliths from mega. *Tectonophysics*, *682*, 186–205. https://doi.org/10.1016/j.tecto.2016.05.027

Török, K., Németh, B., Koller, F., Dégi, J., Badenszki, E., Szabó, C., & Mogessie, A. (2014). Evolution of the middle crust beneath the western Pannonian Basin: A xenolith study. *Mineralogy and Petrology*, *108*(1), 33–47. https://doi.org/10.1007/s00710-013-0287-1

Vaselli, O., Downes, H., Thirlwall, M. F., Dobosi, G., Coradossi, N., Seghedi, I., … Vannucci, R. (1995). Ultramafic xenoliths in Plio-Pleistocene alkali basalts from the eastern Transylvanian Basin: Depleted mantle enriched by vein metasomatism. *Journal of Petrology*, *36*(1), 23–53. https://doi.org/10.1093/petrology/36.1.23

Vaselli, O., Downes, H., Thirlwall, M. F., Vannucci, R., & Coradossi, N. (1996). Spinel-peridotite xenoliths from Kapfenstein (Graz Basin, Eastern Austria): A geochemical and petrological study. *Mineralogy and Petrology*, *57*(1–2), 23–50. https://doi.org/10.1007/BF01161620

Vauchez, A., & Garrido, C. J. (2001). Seismic properties of an asthenospherized lithospheric mantle: Constraints from lattice preferred orientations in peridotite from the Ronda massif. *Earth and Planetary Science Letters*, *192*(2), 235–249. https://doi.org/10.1016/S0012-821X(01)00448-4

Vauchez, A., Dineur, F., & Rudnick, R. (2005). Microstructure, texture and seismic anisotropy of the lithospheric mantle above a mantle plume: Insights from the Labait volcano xenoliths (Tanzania). *Earth and Planetary Science Letters*, *232*, 295–314. https://doi.org/10.1016/j.epsl.2005.01.024

Vauchez, A., Tommasi, A., & Mainprice, D. (2012). Faults (shear zones) in the Earth's mantle. *Tectonophysics*, *558–559*, 1–27.

Vollmer, F. W. (1990). An application of eigenvalue methods to structural domain analysis. *Geological Society of America Bulletin*, *102*(6), 786–791. https://doi.org/10.1130/0016-7606(1990)102%3C0786:AAOEMT%3E2.3.CO;2

Winkler-Hermaden, A. (1957). *Geologisches Kräftespiel und Landformung* (p. 822). Vienna: Springer Verlag. https://doi.org/10.1007/978-3-7091-7881-2

Witt-Eickschen, G., & Seck, H. (1991). Solubility of Ca and Al in orthopyroxene from spinel peridotite: An improved version of an empirical geothermometer. *Contributions to Mineralogy and Petrology*, *106*(4), 431–439. https://doi.org/10.1007/BF00321986

Wright, S. I., Nowell, M. M., & Field, D. P. (2011). A review of strain analysis using electron backscatter diffraction. *Microscopy and Microanalysis*, *17*, 316–329. https://doi.org/10.1017/S1431927611000055

Xia, Q.-K., Hao, Y., Li, P., Deloule, E., Coltorti, M., Dallai, L., … Feng, M. (2010). Low water content of the Cenozoic lithospheric mantle beneath the eastern part of the North China Craton. *Journal of Geophysical Research*, *115*, B07207. https://doi.org/10.1029/2009JB006694

Xia, Q.-K., Hao, Y.-T., Liu, S.-C., Gu, X.-Y., & Feng, M. (2013). Water contents of the Cenozoic lithospheric mantle beneath the western part of the North China craton: Peridotite xenolith constraints. *Gondwana Research*, *23*(1), 108–118. https://doi.org/10.1016/j.gr.2012.01.010

Yang, X.-Z., Xia, Q.-K., Deloule, E., Dallai, L., Fan, Q.-C., & Feng, M. (2008). Water in minerals of the continental lithospheric mantle and overlying lower crust: A comparative study of peridotite and granulite xenoliths from the North China craton. *Chemical Geology*, *256*, 33–45. https://doi.org/10.1016/j.chemgeo.2008.07.020

Yu, Y., Xu, X.-S., Griffin, W. L., O'Reilly, S. Y., & Xia, Q.-K. (2011). H_2O contents and their modification in the Cenozoic subcontinental lithospheric mantle beneath the Cathaysia block, SE China. *Lithos*, *126*, 182–197. https://doi.org/10.1016/j.lithos.2011.07.009

Zaffarana, C., Tommasi, A., Vauchez, A., & Grégoire, M. (2014). Microstructures and seismic properties of south Patagonian mantle xenoliths (Gobernador Gregores and Pali Aike). *Tectonophysics*, *621*, 175–197. https://doi.org/10.1016/j.tecto.2014.02.017

Zhang, S., & Karato, S.-i. (1995). Lattice preferred orientation of olivine aggregates deformed in simple shear. *Nature*, *375*(6534), 774–777. https://doi.org/10.1038/375774a0